Elastic fields around multiple stiff prestressed arcs located on a circle

Zhilin Han[a], Sofia G. Mogilevskaya[b,*], Anna Y. Zemlyanova[c]

[a] *College of Physics, Donghua University, Shanghai, China, 201620*
[b] *Department of Civil, Environmental, and Geo- Engineering, University of Minnesota, 500 Pillsbury Drive S.E., Minneapolis, MN, 55455, USA*
[c] *Department of Mathematics, Kansas State University, 138 Cardwell Hall, Manhattan, Kansas, 66506, USA*

Abstract

The plane strain problem of an isotropic elastic matrix subjected to uniform far-field load and containing multiple stiff prestressed arcs located on the same circle is considered. The boundary conditions for the arcs are described by those of either Gurtin-Murdoch or Steigmann-Ogden theories in which the arcs are endowed with their own elastic energies. The material parameters for each arc can in general be different. The problem is reduced to the system of real variables hypersingular boundary integral equations in terms of two scalar unknowns expressed via the components of the stress tensors of the arcs. The unknowns are approximated by the series of trigonometric functions that are multiplied by the square root weight functions to allow for automatic incorporation of the tip conditions. The coefficients in series are found from the system of linear algebraic equations that is solved using the collocation method. The expressions for the stress intensity factors are derived and numerical examples are presented to illustrate the influence of governing dimensionless parameters.

Keywords: Composites with ultra thin and stiff reinforcements, Gurtin-Murdoch and Steigmann-Ogden theories, Hypersingular integral equations, Stress intensity factors

*Corresponding author
Email addresses: hanzhilin@dhu.edu.cn (Zhilin Han), mogil003@umn.edu (Sofia G. Mogilevskaya), azem@ksu.edu (Anna Y. Zemlyanova)

1. Introduction

In this paper, we study the plane strain problem of an isotropic elastic matrix subjected to uniform far-field load and containing multiple stiff prestressed arcs located on the same circle.

As it has been shown in [1], thin layers of finite thicknesses can be accurately simulated by surfaces of vanishing thicknesses, if the elastic properties of the layers and their thickness are properly chosen. Those authors derived the expressions for the elastic parameters of the surfaces in terms of the properties of the layers they simulate and their thicknesses. It was demonstrated that, for the stiff layers, the displacements are continuous across the simulating surfaces, while the tractions undergo jumps. Later on, several authors, see review in Section 5 of [2], demonstrated that the jump conditions of the [3, 4] and [5, 6] models with zero surface tention coincide with those derived in [1] for the stiff layers of the so-called membrane and shell types.

Therefore, similarly as in earlier publications, see [7–13], it is suggested that the problem under study be modeled using either Gurtin-Murdoch or Steigmann-Ogden theory of material surfaces, if it is assumed that the arcs have vanishing thicknesses and are endowed with their own elastic energies. Such models can be used to simulate a class of composite materials reinforced with thin, stiff, and prestressed layers of the membrane or shell types.

Except for [13], where the plane strain problem of multiple straight thin and stiff prestressed layers was studied, the rest of above mentioned earlier publications were concerned with a problem of a single layer: layers along a straight line were considered in [7–10] and layers along a circular arc were studied in [11, 12]. The focus of the latter two publications was on evaluation of the local fields and comparisons (in case of vanishing surface tension) with the solution given in [14] for the problem of a rigid circular arc. Similar problems with one or even several rigid circular arcs were also considered in [15–17] in plane strain and antiplane settings.

However, it was demonstrated in [11, 12] that, unlike in the case of straight line layer, the circular arc problems described by the Gurtin-Murdoch and Steigmann-Ogden models are never reducible to those of a rigid arc. This is because, according to the classification of [1], the Gurtin-Murdoch and Steigmann-Ogden models with vanishing surface tension represent two distinct interface regimes that are different from the rigid regime. More specifically, the Gurtin-Murdoch model represents the limiting case of the so-called membrane interphase, while the Steigmann-Ogden model that of the inextensible shell interphase.

Here, we generalize the method suggested in [11, 12] to include the case of multiple circular arcs. In addition to evaluation of the local elastic fields, we also derive the expressions for the stress intensity factors (SIFs) at the tips of the arcs and study the far-field signature of the system of arcs, i.e. its imprint on the far away fields.

The paper is structured as follows. In Section 2, we formulate the problem under study. In Section 3, we review the governing equations for the problem, present the governing system of real variables boundary integral equations, and reformulate the system in dimensionless settings. In Section 4, we derive the expressions for the stress intensity factors at the tips of the arcs. In Section 5, we describe major steps of the proposed numerical algorithm. Section 6 contains several examples of numerical simulations. Concluding remarks are presented in Section 7.

2. Problem formulation

Consider the plane strain problem of an isotropic homogeneous elastic plane subjected to uniform far-field load σ^∞ (σ^∞_{11}, σ^∞_{12}, σ^∞_{22}) and containing multiple stiff and prestressed arcs $L^k = (\mathbf{a}^k, \mathbf{b}^k)$, $k = 1, \cdots, K$. Assume that the arcs are located along the same circle of radius R centered at the origin O of the Cartesian coordinate system, so $\mathbf{a}^k = R\exp(\mathrm{i}\beta_1^k)$, $\mathbf{b}^k = R\exp(\mathrm{i}\beta_2^k)$, $\mathrm{i}^2 = -1$, and β_1^k and β_2^k denote the angles associated with the tips of the k-th arc as shown in Fig. 1. Additionally, the local coordinate system with the mutually

orthogonal unit vectors $\boldsymbol{n}$ and $\boldsymbol{\ell}$ is introduced and the notations "+" and "−" identify the regions located from the left (right) of $\boldsymbol{n}$, as shown on the figure.

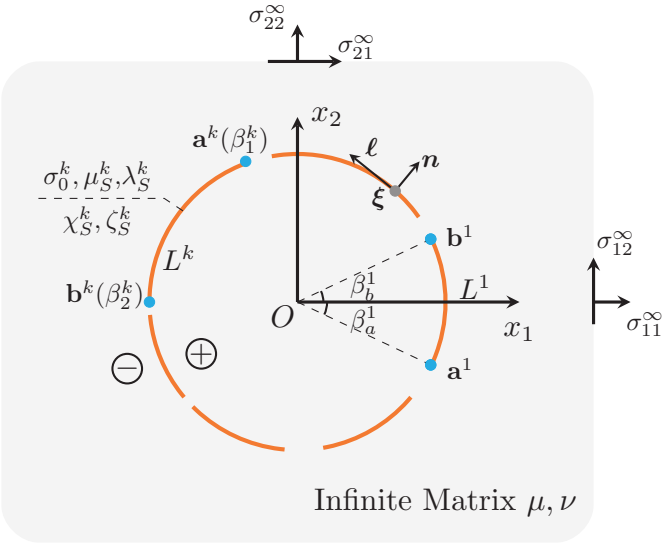

Figure 1: Problem formulation

The elastic properties of the bulk material are given by the shear modulus μ and Poisson's ratio ν and, as stated above, it is assumed that each arc represents a vanishing thickness membrane or shell characterized by its own elastic properties, in accordance with either the Gurtin-Murdoch or Steigmann-Ogden theory. According to both theories, the arc possesses elastic stiffness, characterised by its own Lamé parameters and surface tension, e.g., for the k-th arc they are μ_S^k, λ_S^k, σ_0^k. In the Steigmann-Ogden theory, each arc also possesses bending stiffness characterized for, e.g., k-th arc, by the parameters χ_S^k and ζ_S^k. The latter theory reduces to the Gurtin-Murdoch theory when the bending parameters vanish. We emphasize that the elastic parameters of arcs have dimensions N/m, unlike the elastic parameters of the bulk, whose dimensions are N/m^2. The former elastic parameters are related to the properties of a particular type stiff layer of finite thickness h by the following expressions, see, e.g. [2] and the references therein:

$$\begin{aligned} \lambda_S &= \frac{2\mu_I\lambda_I}{\lambda_I+2\mu_I}h, \quad \mu_S = \mu_I h, \quad \text{membrane type} \\ \lambda_S &= \frac{2\mu_I\lambda_I}{\lambda_I+2\mu_I}h, \quad \mu_S = \mu_I h, \quad (2\chi_S+\zeta_S) = \frac{\mu_I(\lambda_I+\mu_I)}{3(\lambda_I+2\mu_I)}h^3, \quad \text{shell type} \end{aligned} \tag{1}$$

where the subscript I identifies the properties of the layer.

The above expressions are valid when the elastic properties of the layer and its thickness are related as

$$\begin{aligned} &\frac{\lambda_I}{\lambda+2\mu}\frac{h}{H} \sim \Theta(1), \quad \frac{\mu_I}{\lambda+2\mu}\frac{h}{H} \sim \Theta(1), \quad \text{membrane type} \\ &\frac{\lambda_I}{\lambda+2\mu}\left(\frac{h}{H}\right)^3 \sim \Theta(1), \quad \frac{\mu_I}{\lambda+2\mu}\left(\frac{h}{H}\right)^3 \sim \Theta(1), \quad \text{shell type} \end{aligned} \tag{2}$$

in which H is some characteristic length-scale of the problem.

The goals are: i) to evaluate the elastic fields at any point of the material system and stress intensity factors at the tips of the arcs, ii) to study the imprint of the system of arcs on the far-fields (the far-field signature).

3. Basic equations

3.1. Equations of the Gurtin-Murdoch and Steigmann-Ogden theories in plane strain

Under the assumption of isotropy, the behaviour of bulk material in the linearized versions of both theories is governed by the standard Navier equation. Here we additionally assume that the volume forces are zero. The arcs are treated as vanishing thickness material surfaces and the equation for the bulk is supplemented by the conditions describing the behavior of the elastic fields across and at these surfaces.

As the supplementary conditions of the Gurtin-Murdoch theory can be retrieved from those of the Steigmann-Ogden theory by neglecting the bending parameters, we first describe those conditions for the latter theory for the case of material surface L of arbitrary shape with the tips at the points $\boldsymbol{\xi} = \mathbf{a}$ and $\boldsymbol{\xi} = \mathbf{b}$.

The conditions for the fields across L at the point $\boldsymbol{\xi} \in L$ (here and below we omit the argument $\boldsymbol{\xi}$ for brevity) are, see [2, 10, 12],

$$u_1^+ = u_1^- = u_1, \; u_2^+ = u_2^- = u_2, \tag{3}$$

$$\Delta\sigma_n = \sigma_n^+ - \sigma_n^- = -\frac{\sigma^S}{R} + \sigma_0 \frac{\partial \omega^S}{\partial s} - (2\chi_S + \zeta_S)\frac{\partial^3 \omega^S}{\partial s^3}, \tag{4}$$

$$\Delta\sigma_\ell = \sigma_\ell^+ - \sigma_\ell^- = \frac{\partial \sigma^S}{\partial s} + \sigma_0 \frac{\omega^S}{R} - \frac{2\chi_S + \zeta_S}{R}\frac{\partial^2 \omega^S}{\partial s^2}, \tag{5}$$

where u_1 and u_2 are the displacement components of the bulk material in the global coordinate system, σ_n and σ_ℓ are the corresponding normal and shear tractions, $R = R(s)$ is the radius of curvature of L, and s is its arc length. The superscripts "+", "−" here and below describe the limit values of the fields when L is approached from the direction of that of the normal vector or from the opposite direction, respectively. The expressions for the surface strain ε^S and for the components σ^S, ω^S of the surface stress tensor involved in Eqs. (4)-(5) are

$$\varepsilon^S = \frac{u_n}{R} + \frac{\partial u_\ell}{\partial s}, \tag{6a}$$

$$\sigma^S = \sigma_0 + (\lambda_S + 2\mu_S)\varepsilon^S, \tag{6b}$$

$$\omega^S = -\frac{u_\ell}{R} + \frac{\partial u_n}{\partial s}, \tag{6c}$$

in which u_n and u_ℓ are the normal and shear components of the displacements.

The conditions at the tips $\boldsymbol{\xi} = \mathbf{a}$ and $\boldsymbol{\xi} = \mathbf{b}$ of L are given by the following equations:

$$\sigma^S = 0, \tag{7a}$$

$$(2\chi_S + \zeta_S)\frac{\partial \omega^S}{\partial s} = 0, \tag{7b}$$

$$\sigma_0 \omega^S - (2\chi_S + \zeta_S)\frac{\partial^2 \omega^S}{\partial s^2} = 0. \tag{7c}$$

All conditions listed above can be used for each arc L^k, assuming that R is the radius of the circle on which the arcs are located and that the corresponding elastic parameters for each arcs are adopted. The conditions for the Steigmann-Ogden model reduce to those for the Gurtin-Murdoch model when $2\chi_S + \zeta_S = 0$. Thus, in the latter model, the tip condition of Eq. (7b) is automatically satisfied and conditions Eq. (7a) and (7c) state that the only nonzero tangential and normal components of the surface stress tensor σ^S and $\sigma_0\omega^S$ are zero at the tips, see Eq. (40) in [2]. The mechanical meaning of the tip conditions for the Gurtin-Murdoch model is that there are no point forces acting at the surface tips, which would have produced infinite strain energy in the bulk in the vicinity of the tips, see more detailed explanations right after Eq. (18) in [8]. In the Steigmann-Ogden model, Eq. (7b) states that the surface moment is zero at the tips, see Eq. (41) in [2], while Eq. (7c) states that the sum of the normal force due to σ_0 and the shearing force due to bending is zero at each tip, as the derivative of the surface moment is equal to the shearing force.

3.2. Governing integral representations

Natural approach for solving problems involving material surfaces is based on the use of the single layer elastic potential. In such approach, the displacements are sought in the form of the integral over the material surface whose kernel represents the displacements due to the unit force applied at a point on the surface (Kelvin fundamental solution, see, e.g., [18–20]) and the density function can be expressed via the jumps in tractions at that point. With such representation, displacements are continuous across a surface but tractions undergo jumps across it.

For two-dimensional problems, it is beneficial to use the complex variables version of the representation, see [2, 21, 22], that for our problem has the following form:

$$u\left(z\right)=u^{\infty}\left(z\right)-\sum_{k=1}^{K}\frac{1}{4\pi\mathrm{i}\mu\left(\kappa+1\right)}\left\{\int_{L^{k}}\Delta\sigma\left(\tau\right)\left[2\kappa\ln\left(z-\tau\right)-\kappa K_{1}\left(\tau,z\right)\right]\mathrm{d}\tau\right.$$
$$\left.+\int_{L^{k}}\overline{\Delta\sigma\left(\tau\right)}K_{2}\left(\tau,z\right)\mathrm{d}\overline{\tau}\right\}, \tag{8}$$

in which $u=u_1+\mathrm{i}u_2$, $\Delta\sigma=\Delta\sigma_n+\mathrm{i}\Delta\sigma_\ell$, $\kappa=3-4\nu$, $z=z_1+\mathrm{i}z_2$ is a complex variable identifying the point located outside of the arcs, $\tau=\tau_1+\mathrm{i}\tau_2$, a bar over a a symbol denotes complex conjugation,

$$K_1(\tau,z)=\ln\left(\frac{\tau-z}{\overline{\tau}-\overline{z}}\right),$$
$$K_2(\tau,z)=\left(\frac{\tau-z}{\overline{\tau}-\overline{z}}\right), \tag{9}$$

and

$$u^{\infty}(z)=\frac{1}{2\mu}\left[(\kappa-1)\frac{\sigma_{11}^{\infty}+\sigma_{22}^{\infty}}{4}\,z-\frac{\sigma_{22}^{\infty}-\sigma_{11}^{\infty}-2\mathrm{i}\sigma_{12}^{\infty}}{2}\,\overline{z}\right]. \tag{10}$$

The components of the surface stress tensor can be expressed, see [2, 8, 10–12] as

$$\sigma^{S}=\sigma_0^k+(2\mu_S^k+\lambda_S^k)\mathrm{Re}(u'), \tag{11a}$$

$$\omega^{\mathrm{S}}=-\mathrm{Im}(u') \tag{11b}$$

in which σ_0^k, μ_S^k and λ_S^k are the parameters related to L^k, and

$$u'=\frac{\partial u}{\partial z}+\frac{\partial u}{\partial\overline{z}}\frac{\mathrm{d}\overline{z}}{\mathrm{d}z}. \tag{12}$$

Using Eqs. (8), (12) one gets

$$u'(z) = [u^{\infty}(z)]' + \sum_{k=1}^{K} \frac{1}{4\pi \mathrm{i}\mu(\kappa+1)} \left\{ \int_{L^k} \Delta\sigma(\tau) \left[2\kappa \frac{1}{\tau - z} + \kappa \frac{\partial}{\partial z} K_1(\tau, z) \right] \mathrm{d}\tau - \int_{L^k} \overline{\Delta\sigma(\tau)} \frac{\partial}{\partial z} K_2(\tau, z)\, \mathrm{d}\overline{\tau} \right\}, \tag{13}$$

$$[u^{\infty}(z)]' = \frac{1}{2\mu} \left[(\kappa - 1) \frac{\sigma_{11}^{\infty} + \sigma_{22}^{\infty}}{4} - \frac{\sigma_{22}^{\infty} - \sigma_{11}^{\infty} - 2\mathrm{i}\sigma_{12}^{\infty}}{2} \frac{\mathrm{d}\overline{z}}{\mathrm{d}z} \right]. \tag{14}$$

It was shown in [8] that $u'(z)$ is continuous across each arc when $z \to \tau_0$, where $\tau_0 \in \bigcup_{k=1}^{K} L^k$. So, one can combine Eqs. (11) and (13) by using the fact that $\tau = Re^{\mathrm{i}\beta}$ and $\tau_0 = Re^{\mathrm{i}\beta_0}$, see [11, 12], to obtain the following integral equations for the components of the arc's stress tensor at the points on each arc:

$$\begin{aligned} \sigma^S(\beta_0) = {} & \sigma_0^* + (\lambda_S^* + 2\mu_S^*) \operatorname{Re}[u^{\infty}(\beta_0)]' + \\ & \sum_{k=1}^{K} \frac{\kappa(\lambda_S^k + 2\mu_S^k)}{4\pi R\mu(\kappa+1)} \int_{\beta_1^k}^{\beta_2^k} \frac{\sigma^S(\beta)\cos(\beta - \beta_0)}{1 - \cos(\beta - \beta_0)} \mathrm{d}\beta + \\ & \sum_{k=1}^{K} \frac{\kappa(\lambda_S^k + 2\mu_S^k)}{4\pi R\mu(\kappa+1)} \int_{\beta_1^k}^{\beta_2^k} \left[\sigma_0^k \omega^S(\beta) - (2\chi_S^k + \zeta_S^k) \frac{\partial^2 \omega^S(\beta)}{\partial s^2} \right] \frac{\sin(\beta - \beta_0)}{1 - \cos(\beta - \beta_0)} \mathrm{d}\beta + \\ & \sum_{k=1}^{K} \frac{\lambda_S^k + 2\mu_S^k}{4\pi R\mu(\kappa+1)} \int_{\beta_1^k}^{\beta_2^k} \sigma^S(\beta) \mathrm{d}\beta, \end{aligned} \tag{15}$$

$$\begin{aligned} -\omega^S(\beta_0) = {} & \operatorname{Im}[u^{\infty}(\beta_0)]' - \\ & \sum_{k=1}^{K} \frac{\kappa}{4\pi R\mu(\kappa+1)} \int_{\beta_1^k}^{\beta_2^k} \left[\sigma_0^k \omega^S(\beta) - (2\chi_S^k + \zeta_S^k) \frac{\partial^2 \omega^S(\beta)}{\partial s^2} \right] \frac{\cos(\beta - \beta_0)}{1 - \cos(\beta - \beta_0)} \mathrm{d}\beta + \\ & \sum_{k=1}^{K} \frac{\kappa}{4\pi R\mu(\kappa+1)} \int_{\beta_1^k}^{\beta_2^k} \frac{\sigma^S(\beta)\sin(\beta - \beta_0)}{1 - \cos(\beta - \beta_0)} \mathrm{d}\beta + \\ & \sum_{k=1}^{K} \frac{1}{4\pi R\mu(\kappa+1)} \int_{\beta_1^k}^{\beta_2^k} \left[\sigma_0^k \omega^S(\beta) - (2\chi_S^k + \zeta_S^k) \frac{\partial^2 \omega^S(\beta)}{\partial s^2} \right] \mathrm{d}\beta, \end{aligned} \tag{16}$$

in which the superscript $*$ denotes the parameters related to the arc at which $\tau_0 = Re^{\mathrm{i}\beta_0}$ is

located, χ_S^k and ζ_S^k are the bending parameters related to L^k, and

$$\begin{aligned}\mathrm{Re}\left[u^\infty(\beta_0)\right]' &= \frac{1}{2\mu}\left[(\kappa-1)\frac{\sigma_{11}^\infty+\sigma_{22}^\infty}{4} - \frac{2\sigma_{12}^\infty\sin(2\beta_0)+\cos(2\beta_0)(\sigma_{11}^\infty-\sigma_{22}^\infty)}{2}\right],\\ \mathrm{Im}\left[u^\infty(\beta_0)\right]' &= \frac{1}{2\mu}\left[\frac{\sigma_{11}^\infty-\sigma_{22}^\infty}{2}\sin(2\beta_0)-\sigma_{12}^\infty\cos(2\beta_0)\right].\end{aligned} \tag{17}$$

3.3. Dimensionless integral equations

Introducing the following dimensionless parameters:

$$\begin{aligned}\theta^k = \beta_2^k - \beta_1^k,\ \tilde{\sigma}_{ij}^\infty = \frac{\sigma_{ij}^\infty}{\mu},\\ \gamma^k = \frac{\mu R\theta^k}{2\mu_S^k+\lambda_S^k}, \tilde{\sigma}^S = \frac{2\sigma^S}{\mu R\theta^k},\ \tilde{\sigma}_0^k = \frac{2\sigma_0^k}{\mu R\theta^k},\ \tilde{\delta}^k = \frac{8(2\chi_S^k+\zeta_S^k)}{\mu R^3(\theta^k)^3},\\ \Sigma_1(\tau_0) = 2\,\mathrm{Re}\left[u^\infty(\tau_0)\right]',\ \Sigma_2(\tau_0) = \mathrm{Im}\left[u^\infty(\tau_0)\right]'\end{aligned} \tag{18}$$

and the new function $z^S(\beta)$ given by

$$z^S(\beta) = \tilde{\sigma}_0^k\omega^S(\beta) - \frac{(\theta^k)^2\tilde{\delta}_k}{4}\frac{\partial^2\omega^S(\beta)}{\partial\beta^2}, \tag{19}$$

one can rewrite Eq. (15) and Eq. (16) in the dimensionless forms as

$$\begin{aligned}\gamma^*\tilde{\sigma}^S(\beta_0) =& \gamma^*\tilde{\sigma}_0^* + \Sigma_1(\beta_0) + \\ &\sum_{k=1}^K \frac{\kappa\theta^k/2}{2\pi(\kappa+1)}\int_{\beta_1^k}^{\beta_2^k}\frac{\tilde{\sigma}^S(\beta)\cos(\beta-\beta_0)+z^S(\beta)\sin(\beta-\beta_0)}{1-\cos(\beta-\beta_0)}\mathrm{d}\beta + \\ &\sum_{k=1}^K \frac{\theta^k/2}{2\pi(\kappa+1)}\int_{\beta_1^k}^{\beta_2^k}\tilde{\sigma}^S(\beta)\mathrm{d}\beta.\end{aligned} \tag{20}$$

$$\begin{aligned}\omega^S(\beta_0) = -\Sigma_2(\beta_0) + &\sum_{k=1}^K \frac{\kappa\theta^k/2}{4\pi(\kappa+1)}\int_{\beta_1^k}^{\beta_2^k}\frac{z^S(\beta)\cos(\beta-\beta_0)-\tilde{\sigma}^S(\beta)\sin(\beta-\beta_0)}{1-\cos(\beta-\beta_0)}\mathrm{d}\beta - \\ &\sum_{k=1}^K \frac{\theta^k/2}{4\pi(\kappa+1)}\int_{\beta_1^k}^{\beta_2^k} z^S(\beta)\mathrm{d}\beta,\end{aligned} \tag{21}$$

It follows from Eqs. (7c), (18) that

$$z^S(\beta_1^k) = z^S(\beta_2^k) = 0. \tag{22}$$

For the case of a single arc, the details of derivations of Eqs. (20) and (21) can be found in [8, 10–12]. It was shown in [12] that explicit algebraic expression for ω^S as a function of z^S can be obtained by solving differential equation (19) for three different cases (i) $\sigma_0^k > 0$, $2\chi_S^k + \zeta_S^k > 0$; (ii) $\sigma_0^k < 0$, $2\chi_S^k + \zeta_S^k > 0$; (iii) $\sigma_0^k = 0$, $2\chi_S^k + \zeta_S^k > 0$. The results are summarized in Appendix A.

Eqs. (20), (21) and the dimensionalized tip conditions of Eq. (7) remain valid for the case of the Gurtin-Murdoch model, if one assumes that $2\chi_S^k + \zeta_S^k = 0$.

4. Representations for the elastic fields and stress intensity factors

4.1. Representations for the stresses

The tractions $\sigma(z) = \sigma_n(z) + \mathrm{i}\sigma_\ell(z)$ on some line outside of $\bigcup_{k=1}^K L^k$ can be evaluated, see [11, 12], as

$$\sigma(z) = \sigma^\infty(z) - \frac{1}{2\pi\mathrm{i}(\kappa+1)} \sum_{k=1}^K \left\{ \int_{L^k} \Delta\sigma(\tau) \left[(\kappa-1)\frac{1}{\tau - z} + \kappa \frac{\partial}{\partial z} K_1(\tau, z) \right] \mathrm{d}\tau - \int_{L^k} \overline{\Delta\sigma(\tau)} \frac{\partial}{\partial z} K_2(\tau, z)\, \mathrm{d}\overline{\tau} \right\}, \tag{23}$$

where

$$\sigma^\infty(z) = \frac{\sigma_{11}^\infty + \sigma_{22}^\infty}{2} + \frac{\sigma_{22}^\infty - \sigma_{11}^\infty - 2\mathrm{i}\sigma_{12}^\infty}{2} \frac{\mathrm{d}\overline{z}}{\mathrm{d}z}. \tag{24}$$

The Cauchy stresses σ_{ij} can be evaluated using Eq. (23) with the set of appropriately chosen normal vectors. For example, to calculate $\sigma_{11}(z)$ and $\sigma_{12}(z)$, one can set $z = \mathrm{i}x_2$ and assume that normal vector to the line on which z is located (axis Ox_2) points in Ox_1

direction. Thus, $\sigma_n(z) = \sigma_{11}(z)$ and $\sigma_\ell(z) = \sigma_{12}(z)$ on that line. Similarly, to obtain σ_{22}, one can set $z = x_1$ and assume that the normal to the line on which z is located (axis Ox_1) points in Ox_2 direction leading to $\sigma_{22} = \sigma_n$ on that line.

Another way to analytically represent the Cauchy stresses is to use the following Kolosov-Muskhelishvili formulas:

$$\begin{aligned} \sigma_{22}(z) + \mathrm{i}\sigma_{12}(z) &= 2\,\mathrm{Re}\,\Phi(z) + \bar{z}\Phi'(z) + \Psi(z), \\ \sigma_{11}(z) + \sigma_{22}(z) &= 2\left[\Phi(z) + \overline{\Phi(z)}\right], \end{aligned} \tag{25}$$

in which the potentials $\Phi(z)$ and $\Psi(z)$ are taken, see [21, 23], as

$$\begin{aligned} \Phi(z) &= \frac{2\mu u'(z) + \sigma(z)}{\kappa + 1} = \frac{\sigma_{11}^{\infty} + \sigma_{22}^{\infty}}{4} + \frac{1}{2\pi\mathrm{i}(\kappa+1)} \int_L \frac{\Delta\sigma(\tau)d\tau}{\tau - z}, \\ \Psi(z) &= \frac{\sigma_{22}^{\infty} - \sigma_{11}^{\infty} + 2\mathrm{i}\sigma_{12}^{\infty}}{2} + \frac{1}{2\pi\mathrm{i}(\kappa+1)} \int_L \left[\frac{\kappa\overline{\Delta\sigma(\tau)d\tau}}{\tau - z} - \frac{\bar{\tau}\Delta\sigma(\tau)d\tau}{(\tau - z)^2}\right], \end{aligned} \tag{26}$$

with $L = \bigcup_{k=1}^{K} L^k$.

4.2. Stress intensity factors and representations for the stresses near the tips

Consider the case of a material surface along arc L^k with the tips described by the complex variables $\mathbf{a}^k$, $\mathbf{b}^k$ as shown in Fig. 2.

As in, e.g., [23], introduce the local polar coordinate systems $(r, \hat{\theta})$ near the tips using the formulas:

$$z = \mathbf{a}^k + z_1 e^{\mathrm{i}\omega^-}, \;\; z = \mathbf{b}^k + z_1 e^{\mathrm{i}\omega^+}, \tag{27}$$

where $\omega^- = \frac{3\pi}{2} + \beta_1^k$, $\omega^+ = \frac{\pi}{2} + \beta_2^k$ are the angles between the outward tangents at the tips (pointing outside of the material surface) and the positive direction of the x_1-axis of the global coordinate system, and $z_1 = re^{\mathrm{i}\hat{\theta}}$ is the complex coordinate of the point in the local coordinate system for the corresponding tip, as shown on Fig. 2. The branch cut for the square root function $\sqrt{(z - \mathbf{a}^k)(z - \mathbf{b}^k)}$ is made along the material surface with the positive

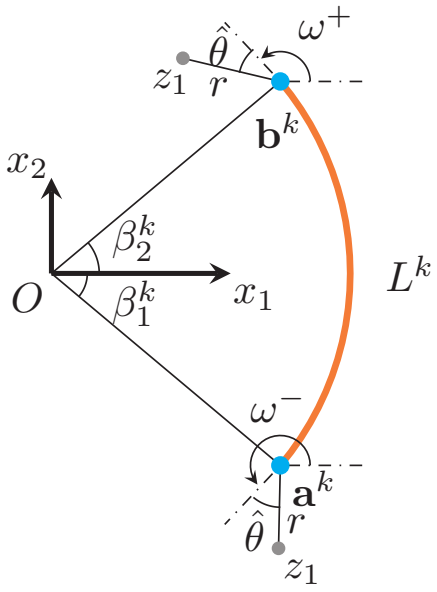

Figure 2: Material surface and local coordinate systems

side of the surface being on the left.

We define the stress intensity factors at the tips as

$$K_1^{\pm} - \mathrm{i}K_2^{\pm} = \lim_{z_1 \to 0} 2\sqrt{2z_1}\Phi(z_1). \tag{28}$$

Taking into account Eq. (28) and singular behavior of the singular integrals of Eq. (26) near the ends of the contour of the integration (reported in, e.g., [24, 23]) we obtain

$$\begin{aligned} \Phi(z_1) &= \frac{K_1^{\pm} - \mathrm{i}K_2^{\pm}}{2\sqrt{2z_1}} + \mathcal{O}(1), \quad z_1 \to 0, \\ \bar{z}_1\Phi'(z_1) + \Psi(z_1) &= \frac{\kappa(K_1^{\pm} + \mathrm{i}K_2^{\pm})}{2\sqrt{2\bar{z}_1}} - \frac{K_1^{\pm} - \mathrm{i}K_2^{\pm}}{4\sqrt{2z_1}}\left(1 + \frac{\bar{z}_1}{z_1}\right) + \mathcal{O}(1), \quad z_1 \to 0. \end{aligned} \tag{29}$$

Substitution of the representations of Eq. (29) into Kolosov-Muskhelishvili formulas (25)

produces the following expressions for the stresses near the tips of the material surface:

$$\begin{aligned}
\sigma_{22}(z_1) &= \frac{K_1^{\pm}}{4\sqrt{2r}}\left[(2\kappa+3)\cos\frac{\hat{\theta}}{2}-\cos\frac{5\hat{\theta}}{2}\right]-\frac{K_2^{\pm}}{4\sqrt{2r}}\left[(2\kappa+3)\sin\frac{\hat{\theta}}{2}-\sin\frac{5\hat{\theta}}{2}\right]+\mathcal{O}(1),\\
\sigma_{12}(z_1) &= \frac{K_1^{\pm}}{4\sqrt{2r}}\left[(2\kappa+1)\sin\frac{\hat{\theta}}{2}+\sin\frac{5\hat{\theta}}{2}\right]+\frac{K_2^{\pm}}{4\sqrt{2r}}\left[(2\kappa+1)\cos\frac{\hat{\theta}}{2}+\cos\frac{5\hat{\theta}}{2}\right]+\mathcal{O}(1),\\
\sigma_{11}(z_1) &= \frac{K_1^{\pm}}{4\sqrt{2r}}\left[-(2\kappa-5)\cos\frac{\hat{\theta}}{2}+\cos\frac{5\hat{\theta}}{2}\right]+\frac{K_2^{\pm}}{4\sqrt{2r}}\left[(2\kappa-5)\sin\frac{\hat{\theta}}{2}-\sin\frac{5\hat{\theta}}{2}\right]+\mathcal{O}(1).
\end{aligned} \tag{30}$$

Eqs. (27)-(30) can be written for each arc L^k. In fact, they will remain valid for any sufficiently smooth arc of arbitrary shape.

The expressions for the dimensionless jumps for the Gurtin-Murdoch (G-M) and Steigman-Ogden (S-O) models can be evaluated from Eqs. (4) and (5) as

$$\text{G-M:}\begin{cases}\Delta\tilde{\sigma}_n(\beta) = -\dfrac{\theta^k}{2}\tilde{\sigma}^S(\beta)+\tilde{\sigma}_0^k\dfrac{\mathrm{d}}{\mathrm{d}\bar{\beta}}\omega^S(\beta),\\ \Delta\tilde{\sigma}_\ell(\beta) = \dfrac{\mathrm{d}}{\mathrm{d}\bar{\beta}}\tilde{\sigma}^S(\beta)+\dfrac{\theta^k\tilde{\sigma}_0^k}{2}\omega^S(\beta),\end{cases} \tag{31a}$$

$$\text{S-O:}\begin{cases}\Delta\tilde{\sigma}_n(\beta) = -\dfrac{\theta^k}{2}\tilde{\sigma}^S(\beta)+\tilde{\sigma}_0^k\dfrac{\mathrm{d}\omega^S(\beta)}{\mathrm{d}\bar{\beta}}-\tilde{\delta}^k\dfrac{\mathrm{d}^3\omega^S(\beta)}{\mathrm{d}\bar{\beta}^3} = -\dfrac{\theta^k}{2}\tilde{\sigma}^S(\beta)+\dfrac{\mathrm{d}}{\mathrm{d}\bar{\beta}}z^S(\beta),\\ \Delta\tilde{\sigma}_\ell(\beta) = \dfrac{\mathrm{d}}{\mathrm{d}\bar{\beta}}\tilde{\sigma}^S(\beta)+\dfrac{\theta^k\tilde{\sigma}_0^k}{2}\omega^S(\beta)-\dfrac{\theta^k\tilde{\delta}^k}{2}\dfrac{\mathrm{d}^2\omega^S(\beta)}{\mathrm{d}\bar{\beta}^2} = \dfrac{\mathrm{d}}{\mathrm{d}\bar{\beta}}\tilde{\sigma}^S(\beta)+\dfrac{\theta^k}{2}z^S(\beta),\end{cases} \tag{31b}$$

in which $\bar{\beta}\in[-1,1]$ can be obtained as the result of the mapping from $\beta\in[\beta_1^k,\beta_2^k]$ given by $\beta=\frac{\theta^k}{2}\bar{\beta}+\frac{\beta_1^k+\beta_2^k}{2}$.

Assuming that the combinations of the surface tensor components for the two models can be represented for the k-th arc as

$$\begin{aligned}
\text{G-M: } \tilde{\sigma}_0^k\omega^S(\beta)+\mathrm{i}\tilde{\sigma}^S(\beta) &= \sqrt{1-\bar{\beta}^2}\mathcal{H}_{\mathrm{GM}}^k(\bar{\beta}),\\
\text{S-O: } z^S(\beta)+\mathrm{i}\tilde{\sigma}^S(\beta) &= \sqrt{1-\bar{\beta}^2}\mathcal{H}_{\mathrm{SO}}^k(\bar{\beta}),
\end{aligned} \tag{32}$$

in which $\mathcal{H}^k(\bar{\beta})$ are sufficiently smooth functions (identified for each model by the corre-

sponding subscript), one can express the stress intensity factors at the points $z = \mathbf{a}^k$, $\mathbf{b}^k$ as

$$K_1^{\pm} - \mathrm{i}K_2^{\pm} = \mp \frac{\sqrt{R\theta^k}}{(\kappa+1)\sqrt{2}} \mathcal{H}^k(\pm 1). \tag{33}$$

The stress intensity factors can be made dimensionless by dividing them by $\sqrt{R/2}$, which leads to the following expression for the normalized stress intensity factors:

$$k_1^{\pm} - \mathrm{i}k_2^{\pm} = \mp \frac{\sqrt{\theta^k}}{\kappa+1} \mathcal{H}^k(\pm 1). \tag{34}$$

5. Major steps of the numerical technique

5.1. Approximations of the unknowns

As in [11, 12], we approximate variables $\tilde{\sigma}^S$, ω^S and z^S on the k-th arc as follows:

$$\begin{aligned} \tilde{\sigma}^S(\bar{\beta}) &= \sqrt{1-\bar{\beta}^2}\, \mathcal{F}^k(\bar{\beta}) \\ &= \sqrt{1-\bar{\beta}^2} \sum_{m=0}^{M} \left\{ A_m^k \cos\left[m \left(\frac{\theta^k}{2}\bar{\beta} + b^k \right) \right] + B_m^k \sin\left[m \left(\frac{\theta^k}{2}\bar{\beta} + b^k \right) \right] \right\}, \end{aligned} \tag{35a}$$

$$\begin{aligned} \omega^S(\bar{\beta}) &= \sqrt{1-\bar{\beta}^2}\, \mathcal{G}_{\mathrm{GM}}^k(\bar{\beta}) \\ &= \sqrt{1-\bar{\beta}^2} \sum_{m=0}^{M} \left\{ D_m^k \cos\left[m \left(\frac{\theta^k}{2}\bar{\beta} + b^k \right) \right] + E_m^k \sin\left[m \left(\frac{\theta^k}{2}\bar{\beta} + b^k \right) \right] \right\}, \end{aligned} \tag{35b}$$

$$\begin{aligned} z^S(\bar{\beta}) &= \sqrt{1-\bar{\beta}^2}\, \mathcal{G}_{\mathrm{SO}}^k(\bar{\beta}) \\ &= \sqrt{1-\bar{\beta}^2} \sum_{m=0}^{M} \left\{ F_m^k \cos\left[m \left(\frac{\theta^k}{2}\bar{\beta} + b^k \right) \right] + G_m^k \sin\left[m \left(\frac{\theta^k}{2}\bar{\beta} + b^k \right) \right] \right\}, \end{aligned} \tag{35c}$$

where A_m^k, B_m^k, D_m^k, E_m^k in Eqs. (35a) and (35b) are the unknown m-th coefficients of the truncated series used for the k-th arc in the case of the Gurtin-Murdoch model, while A_m^k, B_m^k, F_m^k, G_m^k in Eqs. (35a) and (35c) are the corresponding ones in the case of the Steigmann-Ogden model and $b^k = \left(\beta_1^k + \beta_2^k\right)/2$.

It is clear that the use of Eqs. (35a) and (35c) allows for automatic satisfactions of the two tip conditions given by Eqs. (7a) and (7c) for the Steigmann-Ogden model. The remaining tip condition of Eq. (7b), can be used in order to determine the extra coefficients involved in the algebraic relations between z^S and ω^S introduced in Appendix A. Eqs. (35a) and (35b) automatically satisfy the tip conditions of Eqs. (7a) and (7c) for the Gurtin-Murdoch case after the bending parameters are neglected.

Substituting the approximations of Eq. (35) into the system of Eqs. (20), (21) for either the Steigmann-Ogden or the Gurtin-Murdoch model, six types of integrals on the right-hand side of above mentioned equations can be identified. Three types of those integrals are regular integrals, that will be evaluated by using Gaussian quadrature, while the remaining three types are singular and hypersingular integrals and their treatment will follow that discussed in [11, 12].

5.2. Solution of the system and evaluation of the local elastic fields

Standard collocation method is used to generate the system of linear algebraic equations from the governing integral equations (20) and (21). If the series of Eq. (35) are truncated for arc L^k at $m = M$ and K circular arcs are considered, then the total number of unknown coefficients in the series approximations for $\tilde{\sigma}^S$ and z^S (ω^S) for each and all arcs are $4(M+1)$ and $4(M+1)K$ respectively. Special attention should be paid to the case of $\sigma_0^k = 0$ and $2\chi_S^k + \zeta_S^k > 0$ in the Steigmann-Ogden model, where an additional Eq. (A.5) for z^S is required for each arc for obtaining extra unknown coefficient M_4^k in Eq. (A.6), resulting the total number of the equations to be $[4(M+1)+1]K$.

To obtain the unknown coefficients, $2(M+1)$ collocation points are chosen to be uniformly distributed on each arc L^k away from its tips. The approximations of Eq. (35) and determination of extra unknown constant, as explained in Appendix A, automatically satisfy the tip conditions of Eq. (7) in the case of the Steigmann-Ogend model. Approximations

of Eq. (35) also automatically satisfy the tip conditions in the case of the Gurtin-Murdoch model.

The linear system equations are solved by Gaussian Elimination. After the unknown coefficients in Eq. (35) and the unknown constants of Appendix A (for the Steigmann-Ogden model) are obtained, the values of $\tilde{\sigma}^S$ and z^S (ω^S) on each arc can be evaluated.

The normalised stress intensity factors at the tips can be obtained by substituting the approximations of Eq. (35) to Eq. (32), evaluating $\mathcal{H}^k(\bar{\beta})$, and then substituting it into Eq. (33). The final expressions for the k-th arc for both Gurtin-Murdoch and Steigmann-Ogden models are

$$\begin{aligned} \text{G-M: } k_1^{\pm} - \mathrm{i}k_2^{\pm} &= \mp \frac{\sqrt{\theta^k}}{(\kappa+1)} \left[\tilde{\sigma}_0^k \mathcal{G}_{\mathrm{GM}}^k(\pm 1) + \mathrm{i}\mathcal{F}^k(\pm 1)\right] \mathrm{i}, \\ \text{S-O: } k_1^{\pm} - \mathrm{i}k_2^{\pm} &= \mp \frac{\sqrt{\theta^k}}{(\kappa+1)} \left[\mathcal{G}_{\mathrm{SO}}^k(\pm 1) + \mathrm{i}\mathcal{F}^k(\pm 1)\right] \mathrm{i}. \end{aligned} \tag{36}$$

6. Numerical examples

6.1. Influence of interactions

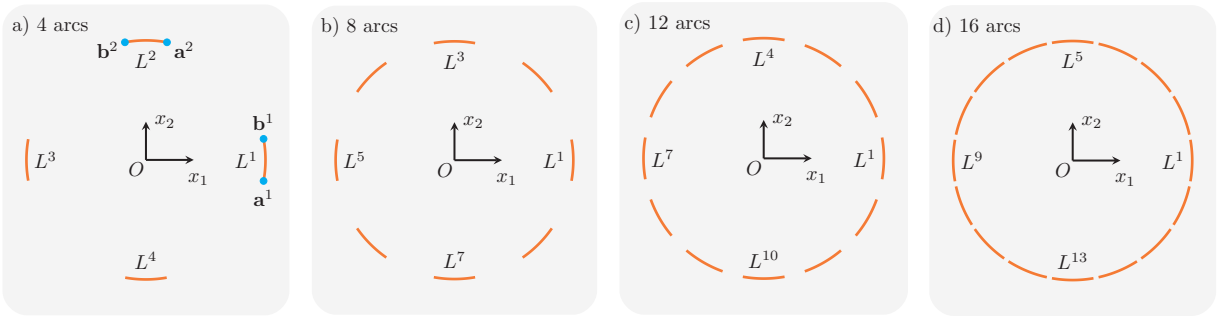

Figure 3: Four arrangements of circular arcs

We start with the case $\tilde{\sigma}_0^k = 0$ and assume that the matrix is characterized by the parameters $\mu = 2$ GPa, $\nu = 0.35$. Assume also that the arcs are arranged symmetrically as shown in Fig. 3 for the cases with $K = 4$, $K = 8$, $K = 12$, $K = 16$. The angle for each arc is taken to be the same ($\theta^k = 20\pi/180$, $k = 1, ..., K$). The interface dimensionless

stiffness parameter for both (Gurtin-Murdoch and Steigmann-Ogden) models is chosen to be $\gamma^k = 0.12$, and the remote loading is taken as $\tilde{\sigma}^{\infty}_{11} = 0.1$. The numerical simulations were performed with the use of the approximations of Eq. (35) truncated at $M = 40$; 800 Gaussian points were used for the evaluation of the regular integrals.

6.1.1. Gurtin-Murdoch model

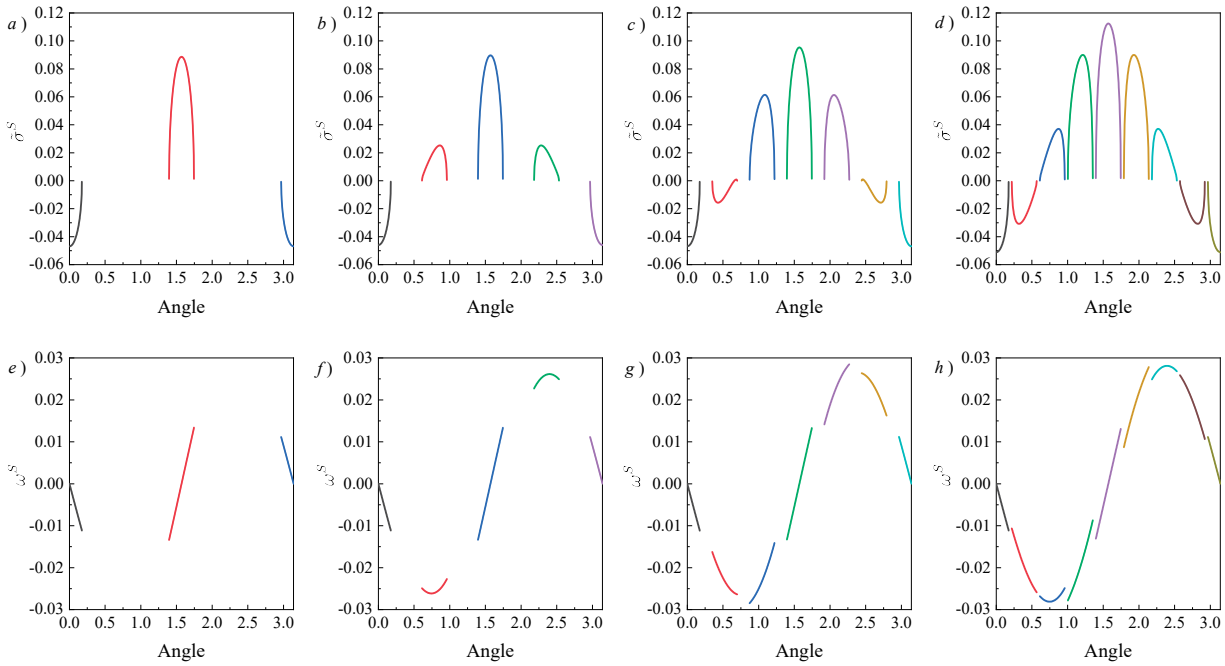

Figure 4: Distributions of $\tilde{\sigma}^S$ and ω^S for $K = 4$, $K = 8$, $K = 12$, and $K = 16$; Gurtin-Murdoch model

The plots of $\tilde{\sigma}^S$ and ω^S for considered values of K are shown in Fig. 4. Due to the symmetry, only values inside the interval $[0, \pi]$ are plotted. We can conclude from the figure that the plots of $\tilde{\sigma}^S$ are symmetric with respect to angle $\pi/2$, while those of ω^S are anti-symmetric. From Figs. 4 a-d, we can also observe that the distribution of $\tilde{\sigma}^S$ is not affected much by the interactions when $K < 8$. However, the effects of interactions become more pronounced with the increase in value of K, which can be especially well seen for the case $K = 16$. Similar conclusions can be drawn by analyzing the plots of ω^S shown on Figs. 4 e-h. It can be observed that $\omega^S \neq 0$ at the tips, as the tip condition of Eq. (7c) is already

satisfied when the bending parameters vanish and $\tilde{\sigma}_0 = 0$.

The components of traction jumps across the arcs for the four arcs arrangements are plotted on the same interval in Fig. 5. Here too, we can see that the plots of $\Delta\tilde{\sigma}_n$ are symmetric with respect to angle $\pi/2$, while those of $\Delta\tilde{\sigma}_\ell$ are anti-symmetric. We can also see that the effects of interactions are getting pronounced when $K \geq 12$. Comparing Figs. 5 a-d with Figs. 4 a-d, we can conclude that the plots of $\Delta\tilde{\sigma}_n$ can be obtained as the results of linear transformations of the corresponding plots of $\tilde{\sigma}^S$ of Fig. 4, which directly follows from Eq. (31a) when $\tilde{\sigma}_0^k = 0$. From Figs. 5e-h, it can be observed that the values of $\Delta\tilde{\sigma}_\ell$ increase dramatically near the tips. This can be again explained by analysing Eq. (31a) for the case $\tilde{\sigma}_0^k = 0$ in which $\Delta\tilde{\sigma}_\ell = \mathrm{d}\tilde{\sigma}^S(\beta)/\mathrm{d}\bar{\beta}$. The latter derivatives, that represent slops of $\tilde{\sigma}^S$, are large near the tips, as it can be seen from Figs. 4a-d.

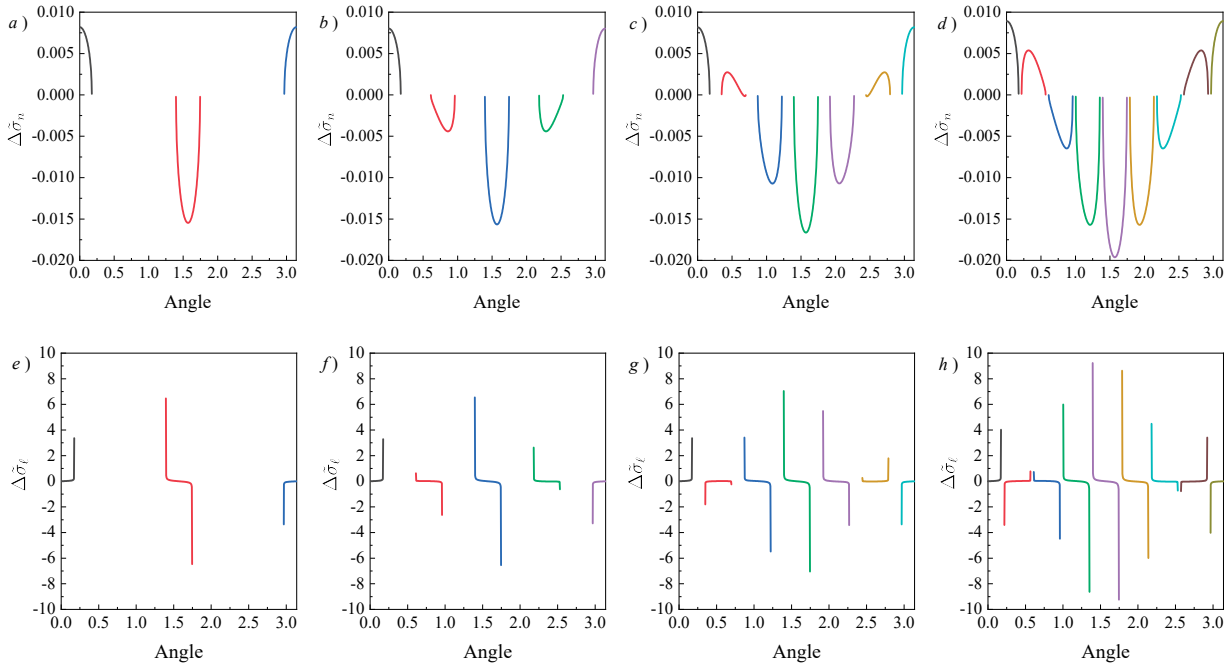

Figure 5: Distributions of $\Delta\tilde{\sigma}_n$ and $\Delta\tilde{\sigma}_\ell$ for $K = 4$, $K = 8$, $K = 12$, and $K = 16$; Gurtin-Murdoch model

The values of the normalised stress intensity factors at the tips of arcs L^k for the four arrangements are presented in Table 1. Due to the symmetry, only part of the values are

Table 1: Normalised stress intensity factors ($\times 10^{-2}$) for the four arrangements; Gurtin-Murdoch model

		L^1	L^2	L^3	L^4	L^5	L^6	L^7	L^8
Fig. 3a	$k_1(\mathbf{a})$	1.0821	-2.0783						
	$k_2(\mathbf{a})$	0.0000	0.0000						
	$k_1(\mathbf{b})$	-1.0821	2.0783						
	$k_2(\mathbf{b})$	0.0000	0.0000						
Fig. 3b	$k_1(\mathbf{a})$	1.0586	-0.1989	-2.1055	-0.8482				
	$k_2(\mathbf{a})$	0.0000	0.0000	0.0000	0.0000				
	$k_1(\mathbf{b})$	-1.0586	0.8482	2.1055	0.1989				
	$k_2(\mathbf{b})$	0.0000	0.0000	0.0000	0.0000				
Fig. 3c	$k_1(\mathbf{a})$	1.0873	0.5811	-1.0983	-2.2691	-1.7615	-0.0837		
	$k_2(\mathbf{a})$	0.0000	0.0000	0.0000	0.0000	0.0000	0.0000		
	$k_1(\mathbf{b})$	-1.0872	0.0844	1.7616	2.2681	1.1002	-0.5804		
	$k_2(\mathbf{b})$	0.0000	0.0000	0.0000	0.0000	0.0000	0.0000		
Fig. 3d	$k_1(\mathbf{a})$	1.2984	1.1016	-0.2337	-1.9230	-2.9765	-2.7801	-1.4449	0.2443
	$k_2(\mathbf{a})$	0.0000	0.0000	0.0000	0.0000	0.0000	0.0000	0.0000	0.0000
	$k_1(\mathbf{b})$	-1.2983	-0.2444	1.4450	2.7801	2.9765	1.9230	0.2337	-1.1015
	$k_2(\mathbf{b})$	0.0000	0.0000	0.0000	0.0000	0.0000	0.0000	0.0000	0.0000

tabulated. It can be seen from Table 1 that $k_2 = 0$ at all tips. One can also find from the table that the values of k_1 at the tips of L^1 (the same arc in all four arrangements) do not change much when $K \leq 12$, which is additional indication that the interactions become more pronounced only when $K > 12$.

6.1.2. Steigmann-Ogden model

For this model, we assume the same material and remote loading parameters as above and additionally assume that $\tilde{\delta}^k = 0.2$.

The plots of $\tilde{\sigma}^S$ and ω^S are shown in Fig. 6 for the four cases of K. Again, due to the symmetry, only values inside the interval $[0, \pi]$ are plotted. Comparison of Fig. 6 with Fig. 4 suggests that the plots of $\tilde{\sigma}^S$ for the Steigmann-Ogden and Gurtin-Murdoch models are practically the same for the considered case of $\tilde{\sigma}_0^k = 0$. Comparison of Figs. 6 and Fig. 4 reveals significant difference in distributions of ω^S for the two models, especially in the vicinity of the tips. This is because, when $\tilde{\sigma}_0^k = 0$, the tip conditions for the Steigmann-Ogden model require that $\partial\omega^S/\partial s = 0$, Eq. (7b), and $\partial^2\omega^S/\partial s^2 = 0$, Eq. (7c), while the tip

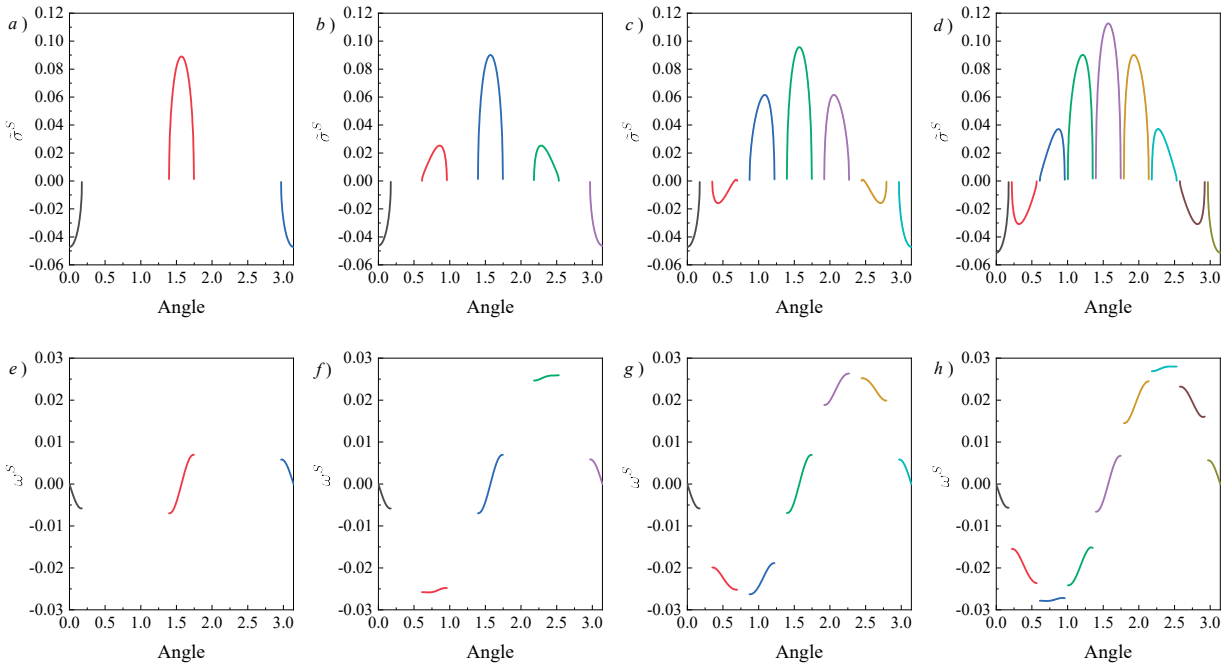

Figure 6: Distributions of $\tilde{\sigma}^S$ and ω^S for $K = 4$, $K = 8$, $K = 12$, and $K = 16$, Steigmann-Ogden model

conditions for the Gurtin-Murdoch model are automatically satisfied when $\tilde{\sigma}_0^k = 0$.

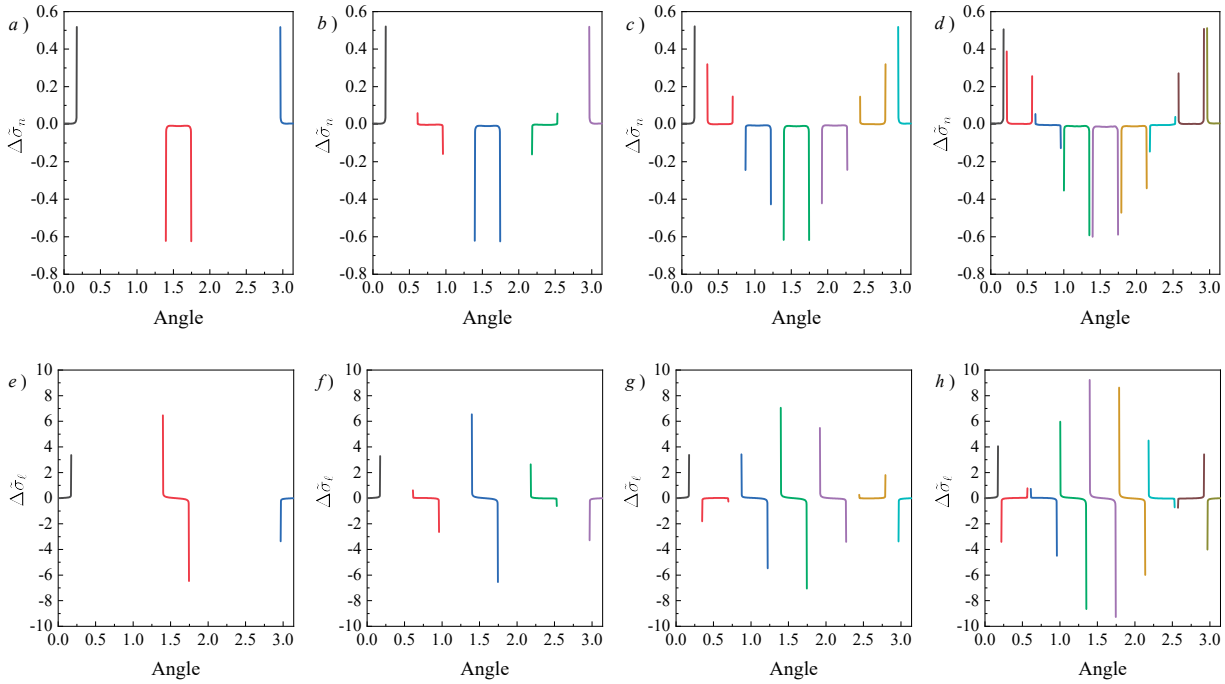

Figure 7: Distributions of $\Delta\tilde{\sigma}_n$ and $\Delta\tilde{\sigma}_\ell$ for $K = 4$, $K = 8$, $K = 12$, and $K = 16$; Steigmann-Ogden model

The components $\Delta\tilde{\sigma}_n$ and $\Delta\tilde{\sigma}_\ell$ of the traction jumps across the arcs inside the interval $[0, \pi]$ are plotted in Fig. 7. We can conclude that the plots of $\Delta\tilde{\sigma}_n$ are symmetric with respect to angle $\pi/2$, while those of $\Delta\tilde{\sigma}_\ell$ are anti-symmetric. From the comparison of Fig. 7 and Fig. 5, it is found that the absolute values of $\Delta\tilde{\sigma}_n$ near the tips for the Steigmann-Ogden model are much larger than the ones for the Gurtin-Murdoch model perhaps because $\Delta\tilde{\sigma}_n$ in the former model is also expressed via $\mathrm{d}^3\omega/\mathrm{d}\bar{\beta}^3$, see Eq. (31b). It can be seen that the behavior of the plots for $\Delta\tilde{\sigma}_\ell$ is practically the same for the two models. This can be explained by analysing Eq. (31b) coupled with the condition $z^S = 0$ at the tips, from which it follows that, as in the Gurtin-Murdoch model, the behavior of $\Delta\tilde{\sigma}_\ell$ near the tips is primarily dominated by that of $\mathrm{d}\tilde{\sigma}^S(\beta)/\mathrm{d}\bar{\beta}$.

Table 2: Normalized stress intensity factors ($\times 10^{-2}$) for the four arrangements; Steigmann-Ogden model

		L^1	L^2	L^3	L^4	L^5	L^6	L^7	L^8
Fig. 3a	$k_1(\mathbf{a})$	1.0816	-2.0777						
	$k_2(\mathbf{a})$	-0.1663	0.2000						
	$k_1(\mathbf{b})$	-1.0816	2.0776						
	$k_2(\mathbf{b})$	-0.1666	0.2007						
Fig. 3b	$k_1(\mathbf{a})$	1.0579	-0.1987	-2.1048	-0.8483				
	$k_2(\mathbf{a})$	-0.1670	-0.0189	0.1999	0.0518				
	$k_1(\mathbf{b})$	-1.0580	0.8483	2.1048	0.1987				
	$k_2(\mathbf{b})$	-0.1675	0.0511	0.2009	-0.0181				
Fig. 3c	$k_1(\mathbf{a})$	1.0866	0.5813	-1.0999	-2.2686	-1.7610	-0.0851		
	$k_2(\mathbf{a})$	-0.1666	-0.1027	0.0786	0.1984	0.1358	-0.0472		
	$k_1(\mathbf{b})$	-1.0867	0.0850	1.7600	2.2669	1.0985	-0.5806		
	$k_2(\mathbf{b})$	-0.1677	-0.0475	0.1375	0.1987	0.0784	-0.1027		
Fig. 3d	$k_1(\mathbf{a})$	1.2881	1.0959	-0.2328	-1.9206	-2.9663	-2.7750	-1.4456	0.2413
	$k_2(\mathbf{a})$	-0.1653	-0.1246	-0.0176	0.1137	0.1931	0.1517	0.0471	-0.0871
	$k_1(\mathbf{b})$	-1.3059	-0.2477	1.4456	2.7816	2.9832	1.9259	0.2325	-1.1022
	$k_2(\mathbf{b})$	-0.1628	-0.0824	0.0412	0.1906	0.1894	0.1100	-0.0126	-0.1634

The values of the normalized stress intensity factors at the tips of the arcs L^k for the four arrangements are presented in Table 2. Here too, only a part of data is tabulated due to the symmetry with respect to angle π. Comparison of Tables 1 and 2 suggests that the values of k_1 at the tips are practically identical for the two models and the main difference

is that $k_2 \neq 0$ for the Steigmann-Ogden model. We can also conclude that the interactions play an important role only when $K > 12$.

6.1.3. Comparison with the single arc results

We observed from Figs. 4 and 6 that, with increase in K, the effects of interactions become more pronounced. To study those effects in more details, we compare the distributions of $\tilde{\sigma}^S$ and ω^S along the arc with angle span $[80\pi/180, 100\pi/180]$, which is present in all four arrangements of Fig. 3. The plots of $\tilde{\sigma}^S$ and ω^S are shown in Fig. 8, both for the Gurtin-Murdoch and Steigmann-Ogden models, and compared with those for the single arc (labeled as $K = 1$), see [11, 12].

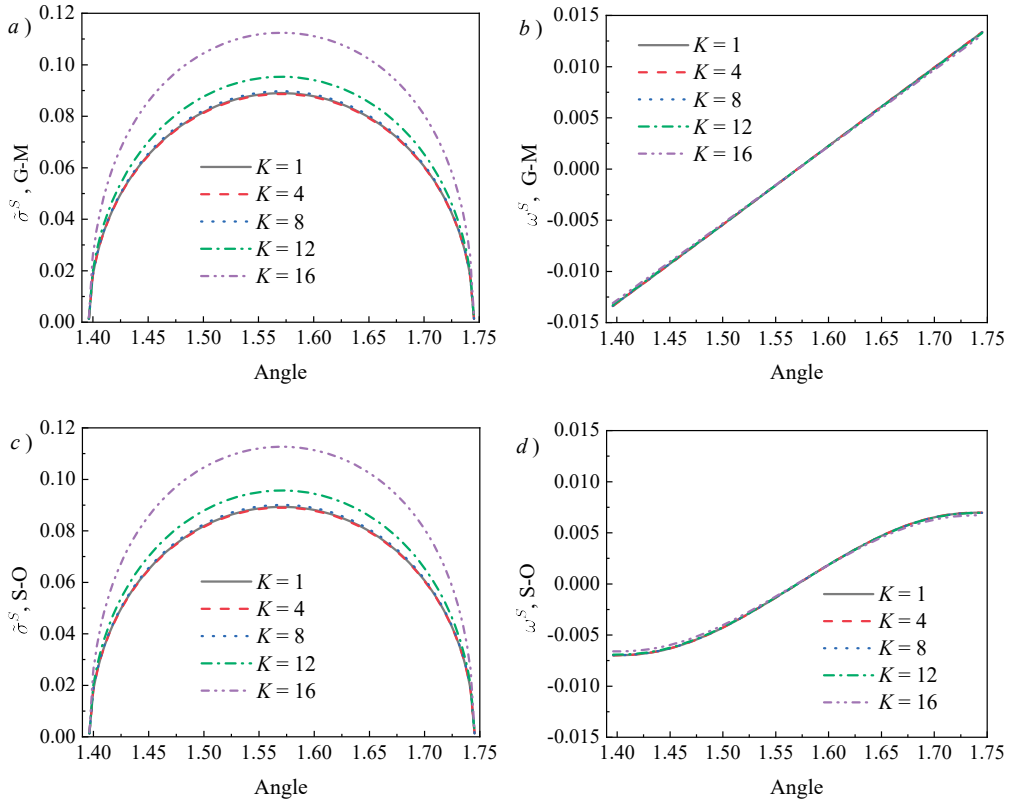

Figure 8: $\tilde{\sigma}^S$ and ω^S along the arc with angle span $[80\pi/180, 100\pi/180]$ for $K = 1$, $K = 4$, $K = 8$, $K = 12$, and $K = 16$

From Figs. 8a and c, we find that the plots of $\tilde{\sigma}^S$ along the considered arc are practically

the same for the Gurtin-Murdoch and Steigmann-Ogden models. It is clear from Figs. 8a, c that, for $K \leq 8$, the plots of $\tilde{\sigma}^S$ practically coincide with the one for the single arc ($K = 1$). With $K \geq 12$, the plots of $\tilde{\sigma}^S$ start to deviate from that for $K = 1$ and the interactions manifest itself by increase in absolute values of $\tilde{\sigma}^S$. From the comparison of Figs. 8b, d, it can be concluded that the plots of ω^S for the Gurtin-Murdoch and Steigmann-Ogden models behave quite differently, perhaps due to the tip conditions of Eqs. (7b) and (7c). It can also be seen that the interactions do not seem effect distributions of ω^S as significantly as those of $\tilde{\sigma}^S$.

We also compared the values of the normalized stress intensity factors at the tips of corresponding arcs. For the Gurtin-Murdoch model, the results from Table 1 for the corresponding four arrangements are $k_1 = \mp 0.0208$, $k_1 = \mp 0.0211$, $k_1 = \mp 0.0227$, $k_1 = \mp 0.0298$ and $k_2 = 0$. The corresponding results for the Steigmann-Ogden model from Table 2 are $k_1 = \mp 0.0208$, $k_1 = \mp 0.0210$, $k_1 = \mp 0.0227$, $k_1 = \mp 0.0297$, which are practically the same as k_1 of the Gurtin-Murdch model, while unlike in the latter model, $k_2 \neq 0$ for the Steigmann-Ogden model. The normalized stress intensity factors for the single arc are $k_1 = \mp 0.0208$ and $k_2 = 0$ for the Gurtin-Murdoch model ([11]), $k_1 = \mp 0.0208$ and $k_2 = 0.0020$ for the Steigmann-Ogden model [12].

6.2. Influences of surface tention

Consider the arrangement of eight arcs shown in Fig. 9 in which $\theta^k = 40\pi/180$ ($k = 1, \cdots, 8$). The matrix is characterized by the same elastic parameters $\mu = 2$ GPa, $\nu = 0.35$ and the remote load is set as $\tilde{\sigma}_{11}^{\infty} = 0.1$. Assume that $\gamma^k = 0.12$ for the two models and consider the following cases of the remaining interfaces parameters for the Gurtin-Murdoch model: (A) $\tilde{\sigma}_0^k = 0.05$; (B) $\tilde{\sigma}_0^k = 0.0$. The following three cases of the remaining interfaces parameters are considered for the Stegimann-Ogden model: (A) $\tilde{\sigma}_0^k = 0.05$, $\tilde{\delta}^k = 0.2$; (B) $\tilde{\sigma}_0^k = 0.0$, $\tilde{\delta}^k = 0.2$; (C) $\tilde{\sigma}_0^k = -0.05$, $\tilde{\delta}^k = 0.2$.

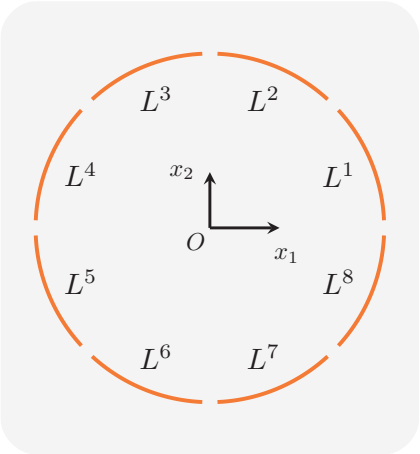

Figure 9: The arrangement with eight arcs

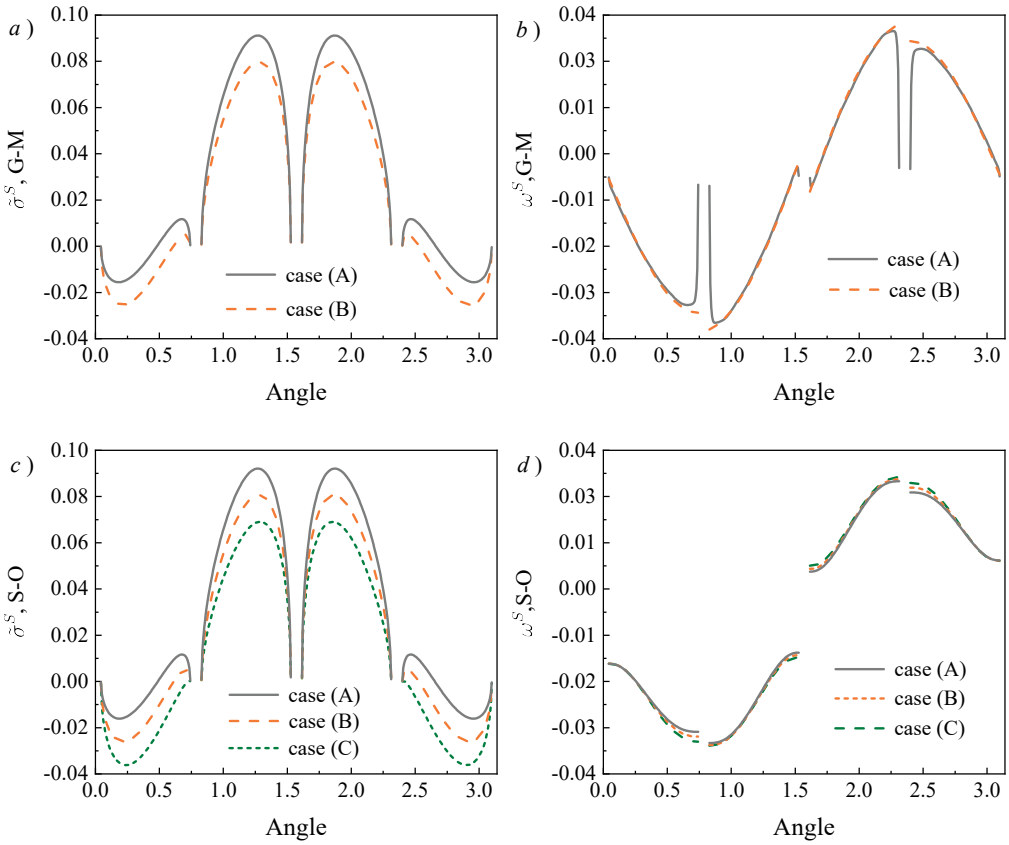

Figure 10: Distributions of $\tilde{\sigma}^S$ and ω^S along L^k $(k = 1, \cdots, 4)$

The plots of $\tilde{\sigma}^S$ and ω^S along the arcs are shown in Fig. 10. Again, only values inside the interval $[0, \pi]$ are plotted from which it can be seen that $\tilde{\sigma}^S$ is symmetric and ω^S is

anti-symmetric with respect to andgle $\pi/2$. It can be observed from Figs. 10a, c that the values of $\tilde{\sigma}^S$ decrease with decrease of $\tilde{\sigma}_0^k$ in all cases considered. From Fig. 10b, we observe that the values of ω^S are not much affected by the surface tension inside most of the interval $[0, \pi]$. However, the plots of ω^S for the cases (A) and (B) of the Gurtin-Murdoch model are significantly different inside two small intervals near the tips, perhaps because ω^S does not have to vanish at the tips for the case (B). From Fig. 10d, we can conclude that the values of ω^S are less influenced by the changes in $\tilde{\sigma}_0^k$ in the three considered cases of the Steigmann-Ogden model.

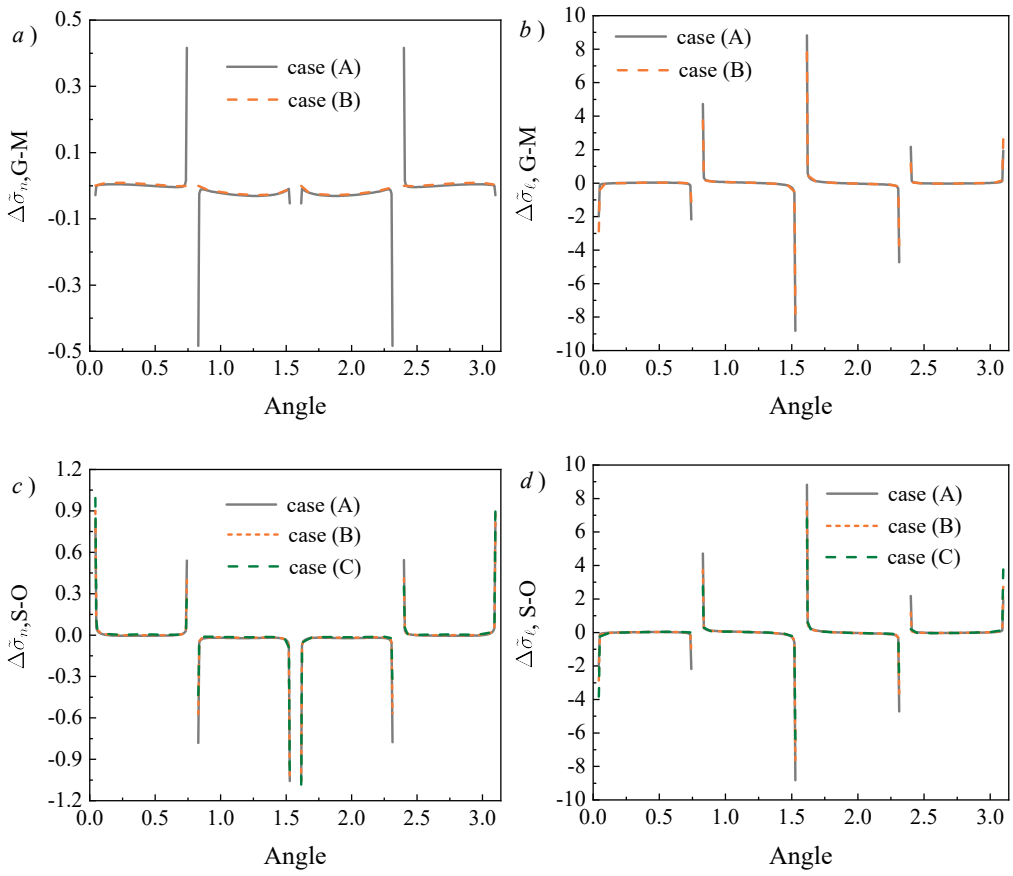

Figure 11: Distributions of $\Delta\tilde{\sigma}_n$ and $\Delta\tilde{\sigma}_\ell$ along L^k $(k = 1, \cdots, 4)$

The components of traction jumps across L^k $(k = 1, \cdots, 4)$ are plotted in Fig. 11, where we find again that the values of $\Delta\tilde{\sigma}_n$ are symmetric and $\Delta\tilde{\sigma}_\ell$ are anti-symmetric with respect

to $\pi/2$. We find from Fig. 11 that the distributions of $\Delta\tilde{\sigma}_n$ and $\Delta\tilde{\sigma}_\ell$, for both the Gurtin-Murdoch and Steigmann-Ogden models, are not influenced by the change in values of $\tilde{\sigma}_0^k$ inside most parts of the interval $[0, \pi]$, except near the arcs tips, where the components of traction jumps decrease with a decrease of $\tilde{\sigma}_0^k$.

6.3. Far-field signature of the arcs

It is known, e.g., [2, 25], that circular inhomogeneities that are fully enclosed by the Gurtin-Murdoch or Steigmann-Ogden material surfaces have the same signatures as equivalent perfectly bonded circular inhomogeneities with appropriately chosen elastic properties. This fact was used in [25, 26] to obtain the overall (effective) properties of the composite materials by employing Maxwell's homogenization scheme.

In order to investigate those signatures, the complementary tractions along some circle of large radius $r \gg R$ were represented by the following complex Fourier series:

$$\underbrace{\tilde{\sigma}(z) - \tilde{\sigma}^{\infty}(z)}_{\text{complementary}} = \tilde{\sigma}_c(z) = \sum_{j=1}^{\infty} A_{-j}(r) g^j(z) + A_0(r) + \sum_{j=1}^{\infty} A_j(r) g^{-j}(z) \tag{37}$$

in which $\tilde{\sigma}_c$ denoted the complementary traction with the normal and tangential components $\tilde{\sigma}_{cn}$ and $\tilde{\sigma}_{c\ell}$, $\tilde{\sigma}_c(z) = \tilde{\sigma}_{cn}(z) + \mathrm{i}\tilde{\sigma}_{c\ell}(z)$, $\tilde{\sigma}^{\infty}(z)$ were obtained from the normalized Eq. (24), $g(z) = r/z$, and A_0, $A_{\pm j}$ were the unknown complex coefficients.

For a single circular inhomogeneity surrounded by either Gurtin-Murdoch or Steigmann-Ogden closed interface, the only meaningful coefficients in the series of Eq. (37) were A_{-2}, A_0, A_2, as the remaining coefficients were practically zero, i.e.

$$\tilde{\sigma}_c(z) = A_{-2}(r) \exp(-2\mathrm{i}\beta) + A_0(r) + A_2(r) \exp(2\mathrm{i}\beta), \tag{38}$$

which meant that the complementary tractions were periodic functions with the period π.

In order to investigate the far-field signature of the circular arcs under study, we consider

four arrangements ($K = 2$, $K = 4$, $K = 6$, and $K = 8$) of arcs separated by the constant angle $5\pi/180$, as shown in Fig. 12. The material parameters of the matrix were taken to be the same as ones introduced in Section 6.2. The interface parameters were also taken to be the same as in the latter section, i.e. cases (A) and (B) for the Gurtin-Murdoch model and (A), (B), (C) for the Steigmann-Ogden model.

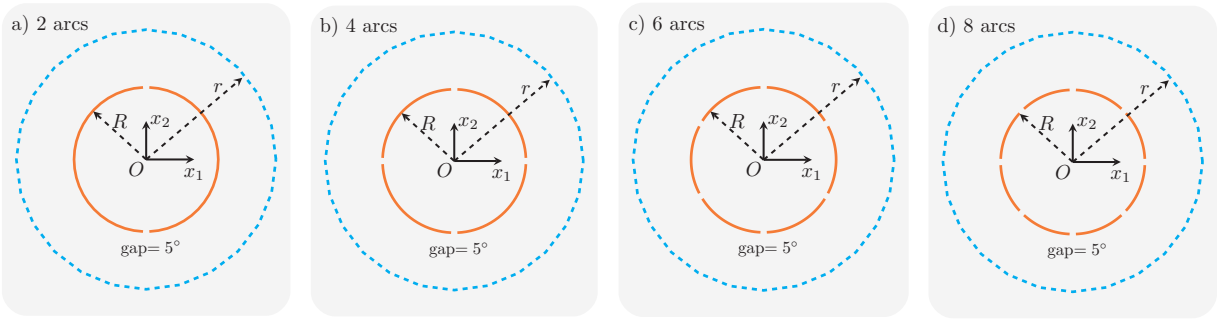

Figure 12: Four arrangements of circular arcs for the studies of far-field signatures

The complementary tractions $\tilde{\sigma}_c$ for the two types of the remote load were evaluated on the circle $r/R = 4$ and decomposed into the series of Eq. (37).

6.3.1. Hydrostatic load

The components of complementary tractions $\tilde{\sigma}_c$ along the circle $r/R = 4$ are plotted in Fig. 13 for the hydrostatic remote load $\tilde{\sigma}^{\infty}_{11} = \tilde{\sigma}^{\infty}_{22} = 0.05$, $\tilde{\sigma}^{\infty}_{12} = 0$. Due to the symmetry, only results inside the interval $[0, \pi]$ are plotted.

It can be observed from Fig. 13 that the normal components $\tilde{\sigma}_{cn}$ are always symmetric with respect to $\pi/2$, while the tangential components $\tilde{\sigma}_{c\ell}$ are anti-symmetric. More importantly, it can be concluded from Fig. 13 that, for both models, the components of complementary tractions are periodic functions whose number of periods inside the interval $[0, 2\pi]$ is always equal to the number K of arcs in the arrangements. This suggests that, for hydrostatic load and $K \geq 4$, the far-field signatures of the arcs for both models are different from the signatures of single circular inhomogeneities surrounded by closed material surfaces,

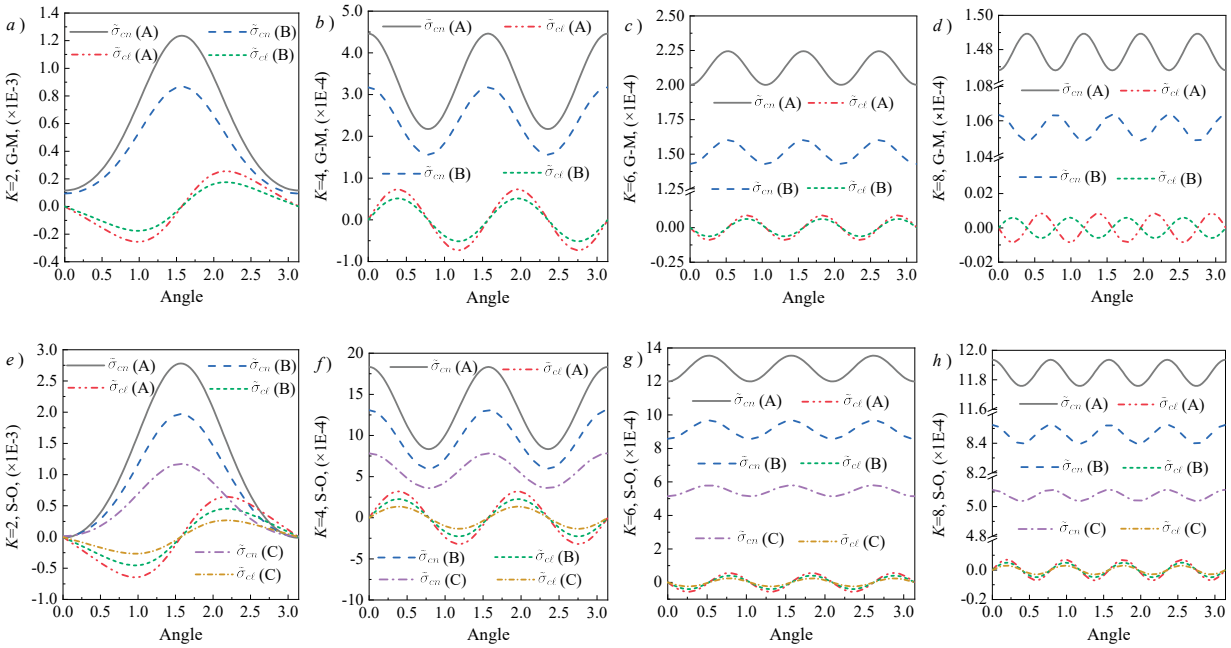

Figure 13: Complementary tractions along the circle $r/R = 4$, hydrostatic remote load.

see, e.g., [25, 27] or from those for circular inhomogeneities with uniform interphase layers, see, e.g., [28, 29]. Additional observation from Fig. 13 is that, for both models, the absolute values of the complementary tractions components for case (A) with $\tilde{\sigma}_0^k = 0.05$ are always larger than the ones for case (B) with $\tilde{\sigma}_0^k = 0$ and for case (C) of the Steigmann-Ogden model with $\tilde{\sigma}_0^k = -0.05$.

6.3.2. Deviatoric load

Consider again the four arrangements of Fig. 12 and take the deviatoric load as $\tilde{\sigma}_{11}^{\infty} = -\tilde{\sigma}_{22}^{\infty} = 0.05$, $\tilde{\sigma}_{12}^{\infty} = 0$.

The components of the complementary tractions $\tilde{\sigma}_c$ along the circle $r/R = 4$ for that case are shown in Fig. 14. Here too, we plot them only inside the interval $[0, \pi]$ due to the symmetry. We see again that the plots of $\tilde{\sigma}_{cn}$ are symmetric, while those of $\tilde{\sigma}_{c\ell}$ are anti-symmetric on that interval.

From Figs. 14a-d, it can be concluded that, for the Gurtin-Murdoch model, the plots for

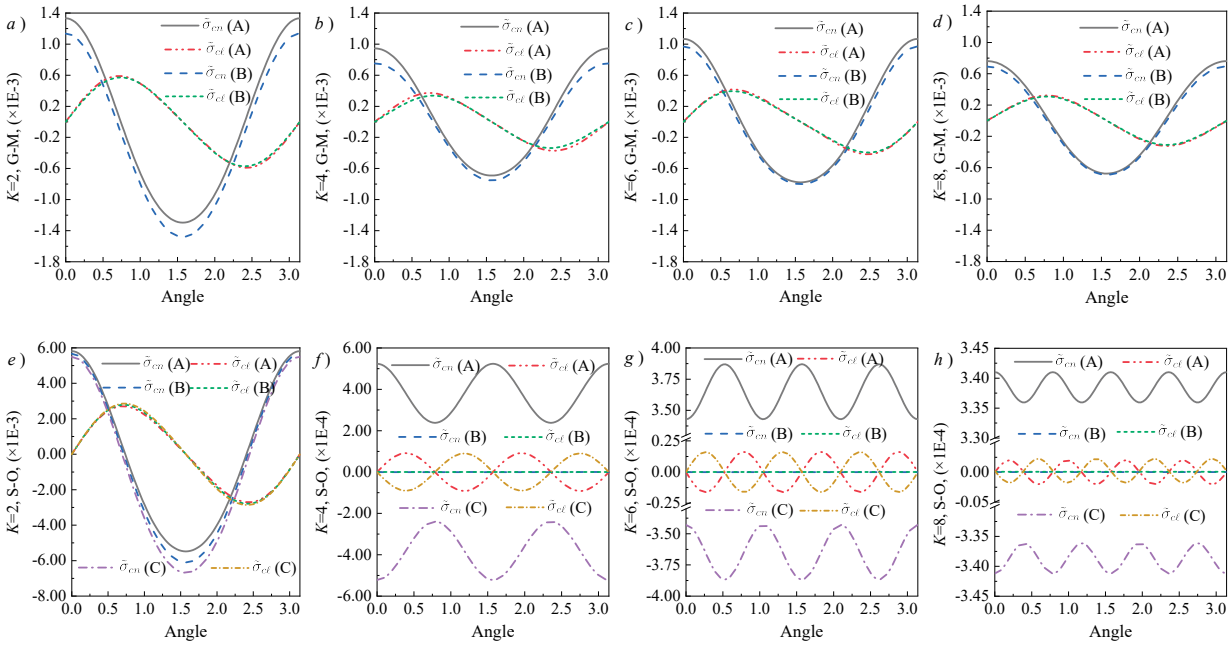

Figure 14: Complementary tractions along the circle $r/R = 4$, deviatoric remote load.

all four arrangements have only one period inside the interval $[0, \pi]$, which suggests that the far-field signatures of $\tilde{\sigma}_c$ are independent on K and are of the type governed by Eq. (38). To study that result further, in Table 3 we tabulated the coefficients A_{-2}, A_{-1}, A_0, A_1, and A_2 obtained using Eq. (37). From that table, we can see that the real parts of A_{-2} and A_2 are the dominant coefficients and the real parts of A_0 for case (A) with the $\tilde{\sigma}_0^k \neq 0$ are not equal to 0, as it should be for a single perfectly bonded inhomogeneity in the case of deviatoric load. This indicates that, for deviatoric load, far-field signatures for the multiple circular arcs in some cases of Gurtin-Murdoch model are still not the same as those in single inhomogeneity model or in the coated circular layer model.

Additionally, it can be observed From Figs. 14a-d that, with the increase in value of K, the absolute values of $\tilde{\sigma}_{cn}$ and $\tilde{\sigma}_{c\ell}$ decrease.

From Figs. 14e-h, we conclude that, for the Steigmann-Ogden model and $K \geq 4$, the components of $\tilde{\sigma}_c$ do have the same number of periods as the number of arcs, similarly to what was observed in the case of hydrostatic load. It can also be observed from the latter

Table 3: Series coefficients for the Gurtin-Murdoch model under deviatoric loads

		2 arcs		4 arcs		6 arcs		8 arcs	
		case A	case B	case A	case B	case A	case B	case A	case B
A_{-2}	Re	3.7E-4	3.7E-4	2.3E-4	2.1E-4	2.6E-4	2.5E-4	2.1E-4	2.0E-4
	Im	4.0E-9	1.0E-9	1.6E-10	1.1E-11	1.4E-8	-8.9E-10	5.8E-8	1.1E-9
A_{-1}	Re	-2.0E-12	-4.0E-12	1.3E-11	-3.4E-12	1.7E-10	-2.5E-12	3.9E-10	7.0E-11
	Im	-5.6E-12	4.5E-12	-1.8E-12	1.1E-12	-4.0E-10	-4.2E-12	2.7E-9	-1.0E-10
A_0	Re	-5.5E-5	-2.2E-4	9.5E-5	-5.0E-11	6.1E-5	3.2E-10	4.2E-5	-2.1E-9
	Im	8.5E-9	2.1E-9	-2.9E-10	-4.0E-12	3.2E-10	-1.8E-10	8.1E-10	-6.6E-12
A_1	Re	2.3E-11	4.7E-11	3.7E-10	-2.1E-12	1.5E-8	2.4E-11	2.1E-8	-2.1E-9
	Im	2.4E-10	-9.2E-12	-2.1E-10	3.5E-12	3.4E-9	9.7E-11	2.8E-8	5.0E-9
A_2	Re	9.5E-4	9.4E-4	6.0E-4	5.5E-4	6.6E-4	6.3E-4	5.2E-4	5.0E-4
	Im	-8.4E-9	-2.4E-9	-4.0E-10	-2.3E-11	-3.6E-8	2.3E-9	-1.5E-7	-2.8E-9

figures that the values of $\tilde{\sigma}_{cn}$ and $\tilde{\sigma}_{c\ell}$ in case (A) (with $\tilde{\sigma}_0^k = 0.05$) are always of opposite signs from the ones in case (C) (with $\tilde{\sigma}_0^k = -0.05$), while the same complementary traction components in case (B) (with $\tilde{\sigma}_0^k = 0$) are zero. However, Fig. 14e for $K = 2$ indicates that the plots of $\tilde{\sigma}_{cn}$ and $\tilde{\sigma}_{c\ell}$ do not have similar characteristics. The latter fact may be due to the large value of $\theta^k > \pi/2$ in case of $K = 2$.

7. Conclusions

In this paper, we studied the plane strain problem of an infinite isotropic elastic matrix subjected to uniform far-field load and containing multiple stiff prestressed arcs located on the same circle. The arcs were modeled as material surfaces described by either Gurtin-Murdoch or Steigmann-Ogden theories. The integral representations for the elastic fields everywhere in the material system were presented and, for the first time, the expressions for the stress intensity factors near the arcs tips were derived. We demonstrated that the numerical technique for solving the problems with a single arc, developed in our earlier publications, could be generalized to allow for accounting for the interactions between multiple arcs. Using this technique, we studied the effects of interactions for various scenarios of dimensionless parameters governing the problem. We also investigated the so-called far-

field signatures of the arcs under various loading conditions. Unlike in the more classical problems of circular inhomogeneities with imperfect interfaces or with uniform interphase layers, which all have dipole signatures (thus allowing for using the concept of an equivalent perfectly bonded inhomogeneity), the signatures of system of multiple arcs turned out to be quite different. In the case of hydrostatic load, the number of multipoles in the multipole expansions of the far-fields always correlated with the number of arcs on a circle, both for the Gurtin-Murdoch and Steigmann-Ogden models. Similar conclusion was reached for the case of deviatoric load and the Steigmann-Ogden model, which was not the case for the same load and the Gurtin-Murdoch model. However, in the latter case, the far-field signatures for the multiple circular arcs in some cases of Gurtin-Murdoch model were still not the same as the classical dipole signatures mentioned above.

Finally, we note that the theoretical developments and the numerical algorithm used in the present paper can be modified and extended to the more general case of the arcs located on different circles and of different radii. More specifically, the relations and integral representations of Eqs. (3)-(14) will remain the same, if one assumes that the local radius of curvature involved in some of those equations is taken to be equal to the radius of the corresponding circle. The changes will appear starting from Eq. (15) in which it was assumed that the center of the circle on which the arcs are located is placed at the origin of the Cartesian coordinate system. The analog of Eq. (15) for the case of arcs on different circles can be obtained by assuming that the expressions for τ and τ_0 on each circle will be changed by adding the complex coordinates of the center of that circle. Such modification will produce additional integrals containing expressions with the coordinates of the centers, but those additional integrals will be of the same types as the ones discussed in the manuscript.

Acknowledgments

Zhilin Han gratefully acknowledges support from the National Natural Science Foun-

dation of China through NSFC No. 12002084. Sofia G. Mogilevskaya gratefully acknowledges the support from the National Science Foundation, United States, award number NSF CMMI-2112894. Anna Y. Zemlyanova gratefully acknowledges the support from the Simons Collaboration Grant for Mathematicians (2020-2025), award number 713080.

Appendix A. Relations between $\boldsymbol{\omega^S}$ and $\boldsymbol{z^S}$ in Steigmann-Ogden theory

The relations are found using standard methods for solving ordinary linear differential equations of the second order, see [12] for the details. The final expressions for the each arc are:

(i) The case $\sigma_0^k > 0$, $2\chi_S^k + \zeta_S^k > 0$,

$$\begin{aligned}\omega^S(\beta^*) =& \frac{2}{\theta^k\sqrt{\tilde{\sigma}_0^k\tilde{\delta}^k}}\int_{\beta_1^k}^{\beta^*} z^S(\beta)\sinh\left(2\sqrt{\frac{\tilde{\sigma}_0^k}{\tilde{\delta}^k}}\frac{\beta-\beta^*}{\theta^k}\right)\mathrm{d}\beta + \\ & \frac{2}{\theta^k\sqrt{\tilde{\sigma}_0^k\tilde{\delta}^k}}\frac{\cosh\left(2\sqrt{\frac{\tilde{\sigma}_0^k}{\tilde{\delta}^k}}\frac{\beta^*-\beta_1^k}{\theta^k}\right)}{\sinh\left(2\sqrt{\frac{\tilde{\sigma}_0^k}{\tilde{\delta}^k}}\right)}\int_{\beta_1^k}^{\beta_2^k} z^S(\beta)\cosh\left(2\sqrt{\frac{\tilde{\sigma}_0^k}{\tilde{\delta}^k}}\frac{\beta-\beta_2^k}{\theta^k}\right)\mathrm{d}\beta,\end{aligned} \tag{A.1}$$

$$\begin{aligned}\frac{\mathrm{d}\omega^S(\beta^*)}{\mathrm{d}\beta^*} =& -\frac{4}{(\theta^k)^2\,\tilde{\delta}^k}\int_{\beta_1^k}^{\beta^*} z^S(\beta)\cosh\left[\frac{2}{\theta^k}\sqrt{\frac{\tilde{\sigma}_0^k}{\tilde{\delta}^k}}(\beta-\beta^*)\right]\mathrm{d}\beta + \\ & \frac{4\sinh\left[\frac{2}{\theta^k}\sqrt{\frac{\tilde{\sigma}_0^k}{\tilde{\delta}^k}}\,(\beta^*-\beta_1^k)\right]}{(\theta^k)^2\,\tilde{\delta}^k\sinh\left(2\sqrt{\frac{\tilde{\sigma}_0^k}{\tilde{\delta}^k}}\right)}\int_{\beta_1^k}^{\beta_2^k} z^S(\beta)\cosh\left[\frac{2}{\theta^k}\sqrt{\frac{\tilde{\sigma}_0^k}{\tilde{\delta}^k}}(\beta-\beta_2^k)\right]\mathrm{d}\beta,\end{aligned} \tag{A.2}$$

in which β^* belongs to the interval $[\beta_1^k,\ \beta_2^k]$.

(ii) The case $\sigma_0^k < 0$, $2\chi_S^k + \zeta_S^k > 0$,

$$\begin{aligned}\omega^S(\beta^*) =& \frac{2}{\theta^k\sqrt{-\tilde{\sigma}_0^k\tilde{\delta}^k}}\int_{\beta_1^k}^{\beta^*} z^S(\beta)\sin\left(2\sqrt{-\frac{\tilde{\sigma}_0^k}{\tilde{\delta}^k}}\frac{\beta-\beta^*}{\theta^k}\right)\mathrm{d}\beta- \\ & \frac{2}{\theta^k\sqrt{-\tilde{\sigma}_0^k\tilde{\delta}^k}}\frac{\cos\left(2\sqrt{-\frac{\tilde{\sigma}_0^k}{\tilde{\delta}^k}}\frac{\beta^*-\beta_1^k}{\theta^k}\right)}{\sin\left(2\sqrt{-\frac{\tilde{\sigma}_0^k}{\tilde{\delta}^k}}\right)}\int_{\beta_1^k}^{\beta_2^k} z^S(\beta)\cos\left(2\sqrt{-\frac{\tilde{\sigma}_0^k}{\tilde{\delta}^k}}\frac{\beta-\beta_2^k}{\theta^k}\right)\mathrm{d}\beta,\end{aligned} \tag{A.3}$$

and

$$\begin{aligned}\frac{\mathrm{d}\omega^S(\beta^*)}{\mathrm{d}\beta^*} =& -\frac{4}{\left(\theta^k\right)^2\tilde{\delta}^k}\int_{\beta_1^k}^{\beta^*} z^S(\beta)\cos\left(2\sqrt{-\frac{\tilde{\sigma}_0^k}{\tilde{\delta}^k}}\frac{\beta-\beta^*}{\theta^k}\right)\mathrm{d}\beta+ \\ & \frac{4}{\left(\theta^k\right)^2\tilde{\delta}^k}\frac{\sin\left(2\sqrt{-\frac{\tilde{\sigma}_0^k}{\tilde{\delta}^k}}\frac{\beta^*-\beta_1^k}{\theta^k}\right)}{\sin\left(2\sqrt{-\frac{\tilde{\sigma}_0^k}{\tilde{\delta}^k}}\right)}\int_{\beta_1^k}^{\beta_2^k} z^S(\beta)\cos\left(2\sqrt{-\frac{\tilde{\sigma}_0^k}{\tilde{\delta}^k}}\frac{\beta-\beta_2^k}{\theta^k}\right)\mathrm{d}\beta.\end{aligned} \tag{A.4}$$

(iii) The case $\sigma_0^k = 0$, $2\chi_S^k + \zeta_S^k > 0$,

$$\int_{\beta_1^k}^{\beta_2^k} z^S(\beta)\mathrm{d}\beta = 0. \tag{A.5}$$

$$\omega^S(\beta^*) = \frac{4}{\left(\theta^k\right)^2\tilde{\delta}^k}\int_{\beta_1^k}^{\beta^*}(\beta-\beta^*)z^S(\beta)\mathrm{d}\beta + M_4^k, \tag{A.6}$$

in which the extra unknown constant M_4^k, have to be determined by solving the system of Eqs. (20) and (21).

References

[1] Y. Benveniste and T. Miloh. Imperfect soft and stiff interfaces in two-dimensional elasticity. *Mech. Mater.*, 33:309–323, 2001. 1

[2] S.G. Mogilevskaya, A.Y. Zemlyanova, and V.I. Kushch. Fiber- and particle-reinforced composite mate-

rials with the Gurtin–Murdoch and Steigmann–Ogden surface energy endowed interfaces. *Appl. Mech. Rev.*, 73(5), 2021. 1, 2, 3.1, 3.1, 3.2, 3.2, 6.3

[3] M.E. Gurtin and A.I. Murdoch. A continuum theory of elastic material surfaces. *Arch. Ration. Mech. Anal.*, 57:291–323, 1975. 1

[4] M.E. Gurtin and A.I. Murdoch. Surface stress in solids. *Int. J. Solids Struct.*, 14:431–440, 1978. 1

[5] D.J. Steigmann and R.W. Ogden. Elastic surface-substrate interactions. *Proceedings of the Royal Society of London. Series A: Mathematical, Physical and Engineering Sciences*, 455(1982):437–474, 1999. 1

[6] D.J. Steigmann and R.W. Ogden. Plain deformations of elastic solids with intrinsic boundary elasticity. *Proc. R. Soc. London A*, 453:853–877, 1997. 1

[7] S. Baranova, S.G. Mogilevskaya, V. Mantic, and S. Jiménez-Alfaro. Analysis of the antiplane problem with an embedded zero thickness layer described by the Gurtin-Murdoch model. *J. Elast.*, 140:171–195, 2020. 1

[8] S.G. Mogilevskaya, A.Y. Zemlyanova, and V. Mantič. The use of the Gurtin-Murdoch theory for modeling mechanical processes in composites with two-dimensional reinforcements. *Compos. Sci. Technol.*, 210:108751, 2021. 3.1, 3.2, 3.2, 3.3

[9] Anna Y Zemlyanova. A problem for a material surface attached to the boundary of an elastic semi-plane. *Math. Mech. Solids*, page 10812865231184415, 2023.

[10] Anna Y. Zemlyanova, Sofia G Mogilevskaya, and Dominik Schillinger. Numerical solution of the two-dimensional Steigmann–Ogden model of material surface with a boundary. *Physica D*, 443(133531), 2023. 1, 3.1, 3.2, 3.3

[11] Z. Han, S.G. Mogilevskaya, and A.Y. Zemlyanova. On the problem of a Gurtin-Murdoch cylindrical material surface embedded in an infinite matrix. *Int.J.Solids Struct.*, 2023. 1, 3.2, 4.1, 5.1, 5.1, 6.1.3, 6.1.3

[12] Zhilin Han, Anna Y Zemlyanova, and Sofia G Mogilevskaya. Two-dimensional problem of an infinite matrix reinforced with a Steigmann–Ogden cylindrical surface of circular arc cross-section. *Int. J. Eng. Sci.*, 194:103986, 2024. 1, 3.1, 3.2, 3.2, 3.3, 4.1, 5.1, 5.1, 6.1.3, 6.1.3, Appendix A

[13] Rohit Satish Patil and Sofia G. Mogilevskaya. Plane strain problem of an elastic matrix containing multiple Gurtin–Murdoch material surfaces along straight segments. *Eng. Anal. Bound. Elem.*, 163:354–368, 2024. 1

[14] Y.W. Liu and C.P. Jiang. Stress distribution at the rigid circular arc inclusion end. *Eng. Fract. Mech.*,

47(3):431–440, 1994. 1

[15] MH Shen and CK Chao. Explicit solutions for the elastic and thermoelastic fields with a rigid circular-arc inclusion. *Int. J. Fracture*, 65:1–18, 1994. 1

[16] CK Chao and SP Wu. Explicit solutions for the antiplane problem of bonded dissimilar materials with two concentric circular-arc inclusions. *J. Energ. Resour. ASME*, 117:1–6, 1995.

[17] You-Wen Liu and Qi-Hong Fang. Plane elastic problem on rigid lines along circular inclusion. *Appl. Math. Mech.*, 26(12):1585–1594, 2005. 1

[18] Carlos Alberto Brebbia, José Claudio Faria Telles, and Luiz C Wrobel. *Boundary element techniques: theory and applications in engineering*. Springer Science & Business Media, 2012. 3.2

[19] MH Aliabadi and PH Wen. *Boundary element methods in engineering and sciences*, volume 4. World Scientific, 2011.

[20] Steven L Crouch and Sofia G Mogilevskaya. *A First Course in Boundary Element Methods*. Springer, 2024. 3.2

[21] A.M. Linkov and S.G. Mogilevskaya. Complex hypersingular BEM in plane elasticity problems. *In: Sladek, V., Sladek, J. (Eds.), Singular Integrals in Boundary Element Method, Chapter 9. Computational Mechanics Publication*, pages 299–364, 1998. 3.2, 4.1

[22] S.G. Mogilevskaya and A.M. Linkov. Complex fundamental solutions and complex variables boundary element method in elasticity. *Comput. Mech.*, 22:88–92, 1998. 3.2

[23] M.P. Savruk. *Two-Dimensional Problems of Elasticity for Bodies with Cracks*. (Naukova Dumka, Kiev) [in Russian], 1981. 4.1, 4.2, 4.2

[24] N.I. Muskhelishvili. *Some Basic Problems of the Mathematical Theory of Elasticity*. Groningen, Noordhoff, 1963. 4.2

[25] A.Y. Zemlyanova and S.G. Mogilevskaya. Circular inhomogeneity with Steigmann-Ogden interface: Local fields, neutrality, and Maxwell's type approximation formula. *Int. J. Solids Struct.*, 135:85–98, 2018. 6.3, 6.3.1

[26] Sofia G. Mogilevskaya, Steven L. Crouch, Alessandro La Grotta, and Henryk K. Stolarski. The effects of surface elasticity and surface tension on the transverse overall elastic behavior of unidirectional nano-composites. *Compos. Sci. Technol.*, 70(3):427–434, 2010. 6.3

[27] Z. Han, S.G. Mogilevskaya, and D. Schillinger. Local fields and overall transverse properties of unidirectional composite materials with multiple nanofibers and Steigmann-Ogden interfaces. *Int. J. Solids Struct.*, 147:166–182, 2018. 6.3.1

[28] SG Mogilevskaya and SL1106 Crouch. A Galerkin boundary integral method for multiple circular elastic inclusions with uniform interphase layers. *Int. J. Solids Struct.*, 41(5-6):1285–1311, 2004. 6.3.1

[29] Sofia G Mogilevskaya, Anna Y Zemlyanova, and Mattia Zammarchi. On the elastic far-field response of a two-dimensional coated circular inhomogeneity: Analysis and applications. *Int. J. Solids Struct.*, 130:199–210, 2018. 6.3.1